Master's thesis

NTNU
Norwegian University of Science and Technology
Faculty of Natural Sciences
Department of Physics

Rasmus André Tranås

Atomistic simulations of thermodynamics and dissolution of iron-silicon phases in iron encasements

Master's thesis in Applied Physics and Mathematics
Supervisor: Jaakko Akola
June 2019

NTNU
Kunnskap for en bedre verden

Rasmus André Tranås

Atomistic simulations of thermodynamics and dissolution of iron-silicon phases in iron encasements

Master's thesis in Applied Physics and Mathematics
Supervisor: Jaakko Akola
June 2019

Norwegian University of Science and Technology
Faculty of Natural Sciences
Department of Physics

NTNU
Norwegian University of
Science and Technology

Abstract

The aim of this Master's thesis is to use density functional theory calculations together with a cluster expansion method, in such a way that iron-silicon alloys on a fixed body-centered cubic lattice can be studied using Monte Carlo simulations in the canonical and semi-grand canonical ensemble. The density functional theory calculations are done using GPAW, and the exchange-correlation functional used is the Perdew-Burke-Ernzerhof functional. Several calculated material properties of iron and silicon are presented, highlighting the capability of density functional theory calculations. Two iron-silicon phases with silicon concentrations of 25 % and 50 % are obtained using Monte Carlo simulated annealing. A phenomenon studied in this thesis is the atomic dissolution of cubes and octahedra, made of the two phases mentioned above, encapsulated in a pure iron phase. It is shown that, in general, higher temperatures are needed to dissolute 50 % of the silicon atoms in the internal structures if the structures are constructed as cubes, as opposed to octahedra. The FeSi phase is found to withstand higher temperatures than the Fe_3Si phase before silicon atoms dissolve into the iron surroundings. Phase boundary tracing is done for low silicon concentrations, showing that there is a temperature and concentration range within which the bcc Fe_3Si and pure iron phases co-exist. The surface energy associated with the intersect between the Fe_3Si and pure iron phases is found to be 99.96 mJ/m^2. This result is obtained from density functional theory calculations with slab structures.

Sammendrag

Målet med denne masteroppgaven er å bruke tetthets-funksjonal-teori sammen med en cluster-ekspansjons-metode, slik at jern-silisium legeringer på et statisk kubisk romsentrert gitter kan bli studert ved bruk av Monte Carlo-simuleringer i det kanoniske og semi-store-kanoniske ensemblet. Tetthets-funksjonal-teori beregningene er gjort med GPAW, og utveksling-korrelasjons funksjonalen brukt er Perdew-Burke-Ernzerhof funksjonalen. Flere beregnede material-egenskaper til jern og silisium er presentert. Dette fremhever mulighetene med tetthets-funksjonal-teori beregninger. To jern-silisium-strukturer med silisium-konsentrasjoner på 25 % og 50 % er funnet ved hjelp av Monte Carlo simulert nedkjøling. Et fenomen studert i denne oppgaven er dissolusjonen av kuber og oktaeder laget av de to ovennevnte fasene plassert i en ren jern-fase. Det er vist at det, i det generelle tilfellet, kreves høyere temperaturer for å dissolvere 50 % av silisium-atomene i den interne strukturen hvis strukturen er konstruert som en kube i stedet for et oktaeder. FeSi-fasen er funnet å motstå høyere temperaturer enn Fe_3Si-fasen før silisium-atomer dissolverer i den omringende jern-fasen. Fase-grense-søk er gjort for lave silisium-konsentrasjoner, som viser at det eksisterer et temperatur- og konsentrasjons-domene hvor bcc Fe_3Si-fasen og den rene jern-fasen eksisterer sammen. Overflateenergien assosiert med et sjikt mellom Fe_3Si- og jern-fasen er funnet til å være 99.96 mJ/m^2. Dette resultatet ble funnet ved å bruke tetthets-funksjonal-teori-beregninger med skive-strukturer.

Preface

This Master's thesis is the grand finale of my Sivilingeniør/Master of Science degree, at the Norwegian University of Science and Technology for the Department of Physics. It concludes a five year integrated degree in Applied Physics and Mathematics, with a specialization in Applied Physics. This project can be considered a continuation of my specialization project (TFY4510), written in the autumn semester of 2018.

The goal of this Master thesis was to develop a cluster expansion based on density functional theory calculations for bcc iron-silicon alloys and further analyze these alloys using Monte Carlo simulations. The motivation for doing this was to better understand the behavior of two iron-silicon phases in iron-rich surroundings and obtain a part of the iron-silicon phase diagram.

I want to thank my supervisor, Professor Jaakko Akola, at the Department of Physics for guiding me while working with this thesis. His curiosity and knowledge of the subject have been essential throughout the academic process, and he has motivated me to keep pushing myself and exploring exciting aspects of material physics. PhD Candidate David Kleiven has helped me execute the required calculations and he has taught me much about relevant physics and scientific methods throughout the last 10 months. For this, I thank him, and I wish him the best of luck in his future endeavors. I would also like to thank Leander Michels, R&D Scientist at Elkem ASA, for having me as a guest while making experimental ferrosilicon trial castings. Lastly, I would like to thank my friends, family, and girlfriend for making my years at NTNU exceed my expectations.

Table of Contents

List of Tables

List of Figures

Abbreviations

fcc - Face-centered cubic

bcc - Body-centered cubic

DOS - Density of states

DFT - Density functional theory

xc - Exchange-correlation

LSDA - Local spin density approximation

LDA - Local density approximation

GGA - Generalized gradient approximation

PBE - Perdew-Burke-Ernzerhof

CE - Cluster expansion

ECI - Effective cluster interaction

CV - Cross-validation

RMSE - Root-mean-square error

MC - Monte Carlo

PAW - Projector augmented wave

MPI - Message passing interface

SOP - Site order parameter

1 Introduction

Metals are found all around, and modern society is dependent on the mass production of metals and alloys to be used in the construction of large scale projects such as railroads and skyscrapers, and the making of transistor-based electronics such as mobile phones and medical devices. This has lead to the need for research and development within the materials industry, where the goals can be to develop new processing techniques to increase production capacity, reduce environmental impacts of processing, or to develop new materials with sought-after properties.

Amongst the most common elements vital for production and development of modern technological appliances are the transition metal iron and the metalloid[1] silicon. Understanding the fundamental properties of these materials is crucial for furthering the technological evolution in such a way that scientists and engineers can construct the solutions of tomorrow. Iron, being one of the most abundant elements on the Earth, has various uses and is extracted and processed at a large scale across the world. Iron can be combined with carbon to form steel, which makes a durable and rigid material, and steel is excellent for making such products as rebars in construction work and drive shafts in the automotive industry. Solid-state devices used in computers and microelectronics are dependent on materials based on silicon, where it enters as a medium for microchip manufacturing. Silicon is also widely used as a semiconductor in modern devices such as solar panels, where silicon is doped to manipulate its electrical properties. Ferrosilicons are iron-silicon alloys with silicon concentrations between 15 and 90 weight percent. These materials have different properties depending on the silicon concentration, therefore entering in many appliances. The more iron-rich alloys in combination with carbon have been extensively used in electrical motors and transformers, due to the magnetic properties, conductivity, and high melting point of the materials. Ferrosilicon is also used as an additive to create silicon steel and stainless steel [2]. In cast iron production ferrosilicon is used as an inoculant [3], changing the microscopic properties of the carbon nucleation in the material [4], drastically altering the properties of the final iron product.

Exploring new macroscopic and microscopic properties of materials has been the goal of materials scientists and physicists for decades, and how experiments for understanding the nature of physical phenomena have been carried out are diverse. As manufacturers and industries are more concerned about the macroscopic properties of materials, it has been the task of the physicists and chemists to explore the fundamentals. This often requires to analyze materials on the atomic level. The exploration of the microstructure of materials can provide a deeper understanding of electronic and chemical reactions, which again is closely linked to macroscopic properties. This research can enhance how materials are produced as well as provide new exotic materials for engineers and manufacturers to apply in their work.

In more recent years the development of supercomputer and cluster technologies has made it

[1] "oides" is a Greek adjectival suffix, and its English derivative form is "oid". The meaning of the word is "being like" or "having the form of" [1, p. 72]. Metalloids have properties in between those of metals and non-metals.

possible to carry out large scale simulations, allowing for increasingly computationally expensive approaches to be viable for solving system equations that in the past would not have been solvable in an appropriate manner. The density functional theory (DFT) has been the backbone of such simulations [5], and has allowed researchers to explore aspects of solids, enhancing how materials are produced in the industry as well as giving scientifically backed information on materials to manufacturers.

The computational resources needed to do DFT calculations increase drastically with the number of atoms in the system, as the scaling is typically $\mathcal{O}(N^3)$. It is therefore not suitable to solely rely on DFT when doing calculations with larger systems. Thus, other computational methods are often utilized to examine larger atomic systems. One method for linking DFT calculations, which are from first principles, to more effective and less time-consuming simulation tools, is with the use of the cluster expansion (CE) method [6]. The first step of this method is to calculate the energy of different atomic configurations on the desired lattice with DFT. A fit can then be made to these energies, where the energy of different clusters in the configurations are coupled with effective cluster interactions (ECIs) to predict the energies. These ECIs can then be used with Monte Carlo (MC) simulations, which in practice makes it possible to study larger atomic systems more efficiently. By employing MC methods, the simulations can be carried out in different statistical ensembles, allowing for thermodynamic properties to be calculated. Thus, macroscopic properties can be extracted, and phase diagrams and free energies can be studied [7].

In this thesis, DFT calculations are done for body-centered cubic (bcc) iron-silicon alloys. These results are used to develop a CE model, and the obtained ECIs are further used in MC simulations. Firstly, Chapter 2 presents important aspects of solid state physics, such as properties of crystalline materials and electronic properties, as well as relevant themes within the fields of DFT, CE, and MC simulations. Chapter 3 sums up the main components of the simulation tools and computational methods used. The obtained results are presented and discussed in Chapter 4, before Chapter 5 concludes the report. Lastly, the thesis ends with suggestions for future work in Chapter 6.

2 Theory

This chapter is comprised of relevant background material for the following chapters and is meant to give insight into some fundamental theoretical aspects of materials science, DFT, CE and MC methods. Some useful concepts from the theory behind crystalline structures, electronic systems, and quantum mechanics are presented, as to lay the foundation for the later discussion regarding material properties of iron and silicon. Some core themes of DFT are included, giving a theoretical base for the computations done and the associated simulation environment. The CE method is also presented, introducing the configurational space for an alloy and the configurational energy. Lastly, the theory behind doing MC simulations in the canonical and semi-grand canonical ensembles for binary alloys is discussed.

2.1 Solid state physics background

This section contains theory from within the field of solid state physics. Theoretical framework of crystalline materials are presented, and [8] is the main reference.

2.1.1 Definition of the crystal system

Within the field of solid state physics an ideal crystal can be described as set of atoms, with a discrete translational symmetry. The group of atoms is periodically repeated in space infinitely, with the same distance between each group. Defining this system in 3 dimensions, the translation vectors, $\mathbf{a}_1, \mathbf{a}_2$ and $\mathbf{a}_3$ are used. These vectors are such that, when viewing the crystal from $\mathbf{r}$ and from $\mathbf{r}' = \mathbf{r} + n_1\mathbf{a}_1 + n_2\mathbf{a}_2 + n_3\mathbf{a}_3$, the lattice will look identical, given that n_1, n_2 and n_3 are integers. $\mathbf{T} = \mathbf{r}' - \mathbf{r}$ thus defines the translation vector of the system.

A unit cell is the smallest cell possible to construct, containing one atom or more, which when repeated infinitely constructs the crystal lattice. The lattice constants describe the physical distance between unit cells. In 3 dimensions there are three lattice constants a, b and c, which may or may not be identical, depending on the crystal lattice symmetry.

The supercell can be constructed by combining several unit cells, thus defining the same overall crystal structure when expanded in space. Even though the unit cell and the supercell describe the same system, the supercell has a larger volume and is among other things used to accurately model crystal defects and crystal vibrations.

2.1.2 Face-centered, diamond and body-centered cubic crystal structures

One common crystal arrangement found in many crystalline materials is the face-centered cubic (fcc) arrangement of atoms. This lattice is constructed as a cube, together with lattice points centered on the faces of the cube. For the fcc lattice system, the lattice constants are equal, such that $a = b = c$. The unit cell is constructed by four lattice points, and its basis is a single atom

located in the origin. In three dimensions the fcc unit cell is defined by the vectors,

$$\mathbf{a}_1 = (\frac{a}{2}, \frac{a}{2}, 0), \quad \mathbf{a}_2 = (\frac{a}{2}, 0, \frac{a}{2}), \quad \mathbf{a}_3 = (0, \frac{a}{2}, \frac{a}{2}). \tag{2.1}$$

If an fcc space lattice is constructed with two identical atoms in the basis at $(0, 0, 0)$ and $(\frac{a}{4}, \frac{a}{4}, \frac{a}{4})$ the structure is called a diamond cubic structure. This arrangement of atoms is commonly found in semiconductors, such as silicon.

Another crystal structure with $a = b = c$ is the bcc structure. This structure is cubic, but with an additional lattice point placed in the center of the cube. The unit cell is constructed by 2 lattice points, and is in three dimensions defined by the vectors,

$$\mathbf{a}_1 = (\frac{a}{2}, \frac{a}{2}, \frac{-a}{2}), \quad \mathbf{a}_2 = (\frac{-a}{2}, \frac{a}{2}, \frac{a}{2}), \quad \mathbf{a}_3 = (\frac{a}{2}, \frac{-a}{2}, \frac{a}{2}). \tag{2.2}$$

At room temperature and below iron has this bcc structure.

In three dimensions the unit cells of the fcc and the bcc structures, as defined by the above-presented vectors, span a volume,

$$V = |\mathbf{a}_1 \cdot \mathbf{a}_2 \times \mathbf{a}_3|, \tag{2.3}$$

where the volume of the fcc unit cell is found to be $V_{\text{fcc}} = a^3/4$, and the volume of the bcc unit cell is $V_{\text{bcc}} = a^3/2$.

2.1.3 Reciprocal lattice and the Brillouin zone

Due to the translational symmetry of the crystal system, any properties within it should be periodic with respect to the lattice, such that $x(\mathbf{r}) = x(\mathbf{r} + \mathbf{T})$. This periodicity of the lattice makes it possible to study the properties of the lattice through its Fourier Transform, called the reciprocal lattice. The periodicity of the lattice in 3 dimensional reciprocal space is represented by the reciprocal translation vectors,

$$\mathbf{b_1} = 2\pi \frac{\mathbf{a}_2 \times \mathbf{a}_3}{\mathbf{a}_1 \cdot \mathbf{a}_2 \times \mathbf{a}_3}, \quad \mathbf{b_2} = 2\pi \frac{\mathbf{a}_3 \times \mathbf{a}_1}{\mathbf{a}_1 \cdot \mathbf{a}_2 \times \mathbf{a}_3}, \quad \mathbf{b_3} = 2\pi \frac{\mathbf{a}_1 \times \mathbf{a}_2}{\mathbf{a}_1 \cdot \mathbf{a}_2 \times \mathbf{a}_3}. \tag{2.4}$$

These vectors are the reciprocal equivalent to the real space lattice vectors, and can construct a translational invariant vector in reciprocal space,

$$\mathbf{G} = m_1\mathbf{b_1} + m_2\mathbf{b_2} + m_3\mathbf{b_3}, \tag{2.5}$$

where m_1, m_2 and m_3 are integers.

When studying the reciprocal lattice, the Brillouin zone is a local area or volume which contains information about the structure of interest. From a reciprocal lattice point in the origin, the Brillouin zone is defined as all points in space closer to the origin than any other

reciprocal lattice point. For a lattice with repeat distance a, the first Brillouin zone is defined as $-\pi/a \leq K \leq \pi/a$, where K is the magnitude of the wave vector. This range for the allowed K, scaling as an inverse of the repeat distance, is a direct result of the Fourier transform, and it follows that the volume of the first Brillouin zone scales as the inverse of the volume of the real space unit cell.

Within the Brillouin zone, several points with a high degree of symmetry are shown to be of particular interest. These points are referred to as critical points. The Γ-point indicates the center of the Brillouin zone [9]. These symmetric points differ between lattice structures, as the reciprocal space representing the lattice structures have different symmetries.

2.2 Electron characteristics and thermodynamics

As the nature of crystal structures and symmetries has been discussed, the next step is to introduce relevant concepts from statistical physics and quantum mechanics to give an introduction to properties of electronic systems. Some aspects of thermodynamics are also discussed, with the motivation to connect microscopic and macroscopic properties of materials. This section uses [8] and [10] as main references.

2.2.1 Bloch functions

In many cases, the Schrödinger equation has to be solved for a periodic potential. If static nuclei are present, their potential can be viewed as such a periodic potential, when solving the equations for a single particle. Bloch's theorem states that the eigenfunctions of a wave subjected to a periodic potential can be expressed as a product of a plane wave and a function containing the periodicity of the lattice, i.e., the periodicity of the fixed nuclei. In mathematical terms, this can be expressed as

$$\psi_{\mathbf{k}}(\mathbf{r}) = u_{\mathbf{k}}(\mathbf{r})e^{i\mathbf{k}\cdot\mathbf{r}}, \tag{2.6}$$

where $u_{\mathbf{k}}(\mathbf{r})$ exhibits the periodicity of the crystal lattice, $u_{\mathbf{k}}(\mathbf{r}) = u_{\mathbf{k}}(\mathbf{r} + \mathbf{T})$, and $\mathbf{T}$ is the translation vector of the system, as discussed in Subsection 2.1.1. Bloch's theorem thus states the translational properties of the wavefunction. With this in mind, it is possible to construct the wavefunction as a Fourier series. Introducing a potential $U(\mathbf{r})$, which is invariant under a lattice translation, and assuming that the crystal is symmetric about $\mathbf{r} = 0$, the potential can be expressed as

$$U(\mathbf{r}) = \sum_{\mathbf{G}} U_{\mathbf{G}} e^{i\mathbf{G}\cdot\mathbf{r}}. \tag{2.7}$$

Here the reciprocal lattice vector, $\mathbf{G}$, is as defined in (2.5), and $U(\mathbf{r})$ is taken to be real. The orbital $\psi(\mathbf{r})$ describes the motion of an electron moving in the external potential, such that the

wave equation becomes

$$\left[\frac{-\hbar^2}{2m}\nabla^2 + \sum_{\mathbf{G}} U_{\mathbf{G}} e^{i\mathbf{G}\cdot\mathbf{r}}\right]\psi(\mathbf{r}) = \epsilon\psi(\mathbf{r}), \tag{2.8}$$

Where ϵ is the energy eigenvalue. By the same logic as for the potential, the wave function can be expressed as a Fourier series summed over allowed values of $\mathbf{k}$, subjected to the boundary conditions,

$$\psi(\mathbf{r}) = \sum_{n,\mathbf{k}} C_{\mathbf{k},n} e^{i\mathbf{k}\cdot\mathbf{r}}. \tag{2.9}$$

This is a packet of Bloch waves, and one Bloch wave can be expressed as

$$\psi_{\mathbf{k},n}(\mathbf{r}) = u_{\mathbf{k},n}(\mathbf{r}) e^{i\mathbf{k}\cdot\mathbf{r}}. \tag{2.10}$$

Again, the periodicity of the lattice is contained in $u_{\mathbf{k},n}(\mathbf{r})$, and the energy eigenstate is represented by n, the energy state, and $\mathbf{k}$, the wave vector of the state. If the solutions for the $C_{\mathbf{k},n}$ are found by obtaining the wave equation (2.9) as a sum, the resulting algebraic equation is the well known Central equation.

2.2.2 Fermi-Dirac distribution

Within the fields of statistical mechanics and quantum mechanics, the use of various distributions is common. For fermions, the Pauli principle states that only two fermions can be in the same quantum state at the same time, and these fermions must have opposing spins. For half-integer spin fermions, such as electrons in thermal equilibrium, the Fermi-Dirac distribution is given as [11, p. 143]

$$F(E) = \frac{1}{e^{(E-\mu_f)/k_B\cdot T} + 1}, \tag{2.11}$$

which is interpreted as the probability of finding an electron in a state with energy E. k_B is the Boltzmann constant, and μ_f is the Fermi level. When the energy, E, is equal to μ_f, $F(E) = 1/2$, such that the Fermi level is the energy at which the probability of finding an electron in a state with energy μ_f is 50%. Also, as the temperature approaches 0 K, the probability of finding an electron with energy higher than the Fermi level becomes zero.

2.2.3 Electronic density of states

The electronic density of states (DOS), $g(E)$, is another distribution from which interesting properties in different systems can be extracted. In short, it describes the number of available states per unit volume per unit energy in an energy interval which states can occupy. In general,

it is given as

$$g(E) = \frac{1}{V} \sum_{n} \sum_{\mathbf{k}} \delta(E - E_n(\mathbf{k})), \tag{2.12}$$

Where n represents the desired energy state or band index, $\mathbf{k}$ is the wave vector and $E_n(\mathbf{k})$ follows from the dispersion relation.

2.2.4 Electron band structure

For a system of electrons, there exist restrictions depending on the system, which differentiates between allowed and forbidden electron energies. These regions of allowed energies are called bands and are derived from the allowed wave functions of the electrons in the energy region. For each $\mathbf{k}$, as in Equation (2.10), there can exist several energy states, n, which can be used to obtain the energy state dispersion relation for electrons in the band n. In 3 dimensions, the Brillouin zone has different shapes depending on the system. It is therefore common to view the electronic bands along directions of high symmetry, the so-called critical points.

To categorize different systems, the electron bands can be analyzed. Metals have the Fermi level, μ_f, inside one or more bands, and semiconductors, as well as insulators, have μ_f in so-called forbidden regions between bands. For metals, having the Fermi level inside a band corresponds to metals having bands which are partially filled with electrons.

2.2.5 Energy of formation

When chemical reactions occur, it is interesting to look at the energy needed for an endothermic reaction or the energy released for an exotherm reaction when reactants combine to form products and to examine whether the formed products are energetically favorable or not, compared to the separate reactants. The enthalpy of formation can be thought of as the change in enthalpy when two or more elements combine to form a substance [12]. More precisely, it is the difference between the enthalpy of formation for the products and the reactants. Hess' law gives this change in formation enthalpy as

$$\Delta H^0_{\text{Reaction}} = \Delta H^0_f(\text{Products}) - \Delta H^0_f(\text{Reactants}), \tag{2.13}$$

where superscript 0 indicate that an equilibrium state is reached. A similar logic can be used to examine whether two or more atoms forming an alloy combine or segregate. The enthalpy is defined as

$$H = U + pV, \tag{2.14}$$

where U is the internal energy of the system, p is the pressure, and V is the volume. If the system is equilibrated to a state where $p = 0$, the enthalpy is equal to the systems internal energy. This

can again be used to express the formation energy. For an alloy consisting of two atom types i, j and $N = N_j + N_i$ atoms in the cell, the energy of formation can be expressed as

$$E_{\mathrm{f}} = E_{\mathrm{b}}^{\mathrm{alloy}} - \mathrm{X}(i)E_{\mathrm{b}}^{i} - \mathrm{X}(j)E_{\mathrm{b}}^{j}. \tag{2.15}$$

Here the atomic concentrations of element i and j are X(i) = N_i/N and X(j) = N_j/N, and subscript b indicate that the energies are for the bulk. The energies on the right hand side are total energy of the alloy, the total energy of the bulk of N atoms of type i, and the total energy of the bulk of N atoms of type j respectively. A negative formation energy corresponds to an alloy structure which is energetically favorable compared to the bulk consisting only of the segregated elements i and j.

2.2.6 Free energy and heat capacity

At constant temperature, a physical system such as an alloy will try to minimize its free energy. Calculating the free energy thus gives information about the direction of the reactions happening as an equilibrium is reached. The Gibbs free energy can be expressed as [13, p. 72]

$$G = U + pV - TS = H - TS, \tag{2.16}$$

where U is the internal energy, p is the pressure, V is the volume, T is the temperature, and H and S are the enthalpy and entropy of the system respectively. This free energy is a measure of the amount of reversible work that can be performed at constant p and T. The Gibbs free energy can be used to identify stable states and phase equilibria in alloys. From the second law of thermodynamics it is known that a state is stable if and only if it minimizes the Gibbs free energy at constant p and T [14]. At a composition X this would mean reducing $G(X)$. The system may however reduce the Gibbs free energy by splitting into phases. If the composition X is split into two phases, one with composition X_i of fraction f_1 and one with composition X_j of fraction $f_2 = 1 - f_1$, the Gibbs free energy of the two-phase system, $G_{\mathrm{sys}}(X)$, can be written as

$$G_{\mathrm{sys}}(X) = f_1 G(X_1) + f_2 G(X_2), \tag{2.17}$$

where $X = f_1 X_1 + f_2 X_2$. It follows that if $G_{\mathrm{sys}}(X) < G(X)$ it is energetically favorable for the system to split in the two phases. For the Gibbs free energy to be minimized, all possible phases and combinations of phases must be considered. This concept of investigating the Gibbs free energy for different phases gives rise to the convex hull, which can be used to identify phase equilibria or ground states [15]. It should be noted that at $T = 0$ and $p = 0$, the Gibbs free energy (2.16) is simply the internal energy of the system, and the phase exploration can be done using the formation energy as discussed in Subsection 2.2.5.

If the system is not subjected to any pressure, the Gibbs free energy (2.16) reduces to the

Helmholtz free energy,

$$F = U - TS. \tag{2.18}$$

The partition function for the canonical ensemble, Z, is defined as [11, p. 55]

$$Z = \sum_i e^{-\beta E_i}, \tag{2.19}$$

where $\beta = \dfrac{1}{k_\mathrm{B}T}$, E_i is the total energy of microstate i, and the sum over i represents a summation over all possible microstates of the system. At zero pressure the relationship between this partition function and the internal energy is [11, p. 58]

$$Z = e^{-\beta F}, \tag{2.20}$$

and the connection between the partition function and the internal energy is [11, p. 56]

$$U = -\frac{1}{Z}\frac{\partial Z}{\partial \beta} = -\frac{\partial \ln Z}{\partial \beta}. \tag{2.21}$$

Combining equations (2.20) and (2.21) by inserting Z, taking the natural logarithm and differentiating, the result can be written as

$$U = \frac{\mathrm{d}}{\mathrm{d}\beta}(\beta F). \tag{2.22}$$

Integrating this over a range of β, with a corresponding temperature range yields

$$\int_{\beta_0}^{\beta_1} \mathrm{d}\beta U = \beta_1 F_1 - \beta_0 F_0 \tag{2.23}$$

Thus, F_1 can be expressed as

$$F_1 = \frac{\beta_0 F_0}{\beta_1} + \frac{1}{\beta_1}\int_{\beta_0}^{\beta_1} \mathrm{d}\beta U, \tag{2.24}$$

where the integral can be computed numerically, and has to be evaluated at each β_1 corresponding to a temperature T_1. When F_1 is computed, Equation (2.18) can be used to calculate the entropy for a given temperature when the system is subjected to zero pressure.

Another thermodynamic quantity describing the state of a system and the way it behaves when a change in temperature occurs is the heat capacity, $C_V(T)$. The heat capacity is defined as the amount of energy required to be added to a system to increase its temperature by 1 K in equilibrium. It is therefore related to the internal energy of the system [13, p. 28],

$$C_V(T) = \left(\frac{\partial U}{\partial T}\right)_{V,N}, \tag{2.25}$$

where the subscripts V and N indicate that it is the heat capacity at constant volume and

constant number of particles respectively. Through thermodynamic relations, $C_V(T)$ can also be expressed through the change in entropy [13, p. 54],

$$C_V(T) = T\left(\frac{\partial S}{\partial T}\right)_{V,N}, \tag{2.26}$$

showing that the heat capacity is directly related to the change in the disorder of the system.

2.2.7 Surface energy

While the formation energy and Gibbs free energy are helpful to understand why ground states occur and why different phases are observed in alloys, the surface energy is important when studying the interface between different phases. The shape and the size of phase clusters, as well as the number of clusters located inside a bulk material, is crucial for macroscopic material properties [16]. When combining two phases, the surface energy can be analyzed to understand why two phases co-exist, or why the phases dissolve. n-layer thick slabs of the two combined phases can be used for calculating the surface energy. n then represents the thickness of one of the phases in the slab, where both phases have the same sized cell. Defining E_n as the total energy associated with one such n-layer slab, the surface energy, $E_s(n)$, can be expressed as [17],

$$E_s(n) = \frac{1}{2}\left(E_n - 2\Delta E(n)\right), \tag{2.27}$$

where $\Delta E(n) = E_n - E_{n-1}$. The 1/2 is introduced as with periodic boundary conditions the slab has two surfaces. As the slab size is associated with a surface area between the two phases in the slab, the surface energy per area can be defined as

$$\gamma = E_s(n)/A_s, \tag{2.28}$$

where A_s is the area of the intersection between the two phases.

2.3 Magnetic systems and the Schrödinger equation

This section contains aspects regarding quantum mechanical interactions of electrons and nuclei and is largely based on [10]. The theory is laid out in such a way to demonstrate magnetic phenomenon and the complexity and demands of solving the many-body interacting particle equations.

2.3.1 Magnetism

Free atoms have a magnetic moment, which arises from three different quantum mechanical effects, namely the electron spins, the electrons orbital angular momentum and the change in the orbital momentum stemming from an applied magnetic field. In the absence of an external

magnetic field, the magnetic moment of an atom is given by

$$\boldsymbol{\mu} = -g\mu_B \mathbf{J}, \tag{2.29}$$

where $\mathbf{J}$ is the sum of orbital and spin angular momenta. g, or the g factor, stems from the Landé equation [8, p, 302], and μ_B is the Bohr magneton,

$$\mu_B = \frac{e\hbar}{2m_e}. \tag{2.30}$$

The Bohr magneton is a natural constant, where e is the electron charge, m_e is the electron mass, and $\hbar$ is the reduced Planck constant. The Bohr magneton constant represents the unit magnetic moment. Defining the magnetization, M, as the magnetic moment per unit volume, the magnetic susceptibility per unit volume is

$$\chi = \frac{\mu_0 M}{B}. \tag{2.31}$$

Here B is the intensity of the macroscopic magnetic field, and μ_0 is the permeability of free space. A material with positive χ is called paramagnetic, meaning that if the substance is in the proximity of an applied magnetic field, the induced magnetization in the substance will be directed in the same direction as the applied field. If the induced magnetization in the substance points in the opposite direction as the applied field, χ is less than zero, and the material is diamagnetic. Paramagnetic and diamagnetic substances have no induced magnetization in the absence of an external magnetic field, as the magnetic moments of the materials are randomly oriented due to thermal fluctuations. Ferromagnets, on the other hand, have a magnetic moment, and thus non-zero magnetization in zero external magnetic field. In the presence of an external magnetic field, the magnetization of a ferromagnetic material will be magnified if the magnetic moments in the material are oriented in the same direction as the external field. Figure 2.1 illustrates the above mentioned magnetic properties of the materials discussed.

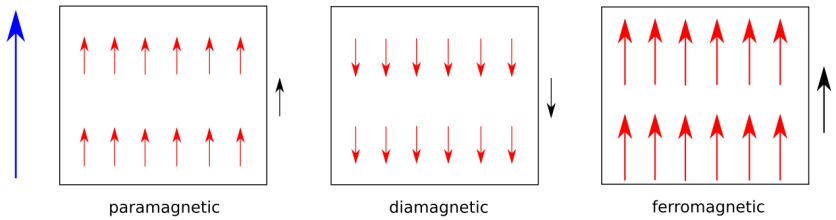

Figure 2.1: Magnetization and magnetic susceptibility for paramagnetic, diamagnetic and ferromagnetic materials in an external magnetic field. The blue arrow indicates the applied magnetic field, the red arrows show the magnetization, and the black lines show the resulting magnetic susceptibility. The size of the arrows indicate the intensity.

2.3.2 Particle interactions and the wave function

To solve the system equations for a system involving several atoms, with many nuclei and even more electrons, the starting point is the time-independent many-body Schrödinger equation. The time-independent Schrödinger equation can be evaluated here, as the ground state energy is time independent. To get the energy eigenvalues, one must therefore consider

$$\hat{H}\Psi(\mathbf{x_1}, ..., \mathbf{x_n}) = E\Psi(\mathbf{x_1}, ..., \mathbf{x_n}), \tag{2.32}$$

where E the ground state energy and $\psi(\mathbf{x_1}, ..., \mathbf{x_n})$ is the many-body stationary wave function. Note that the coordinate $\mathbf{x}_i$ contains spin as well as position for the particles. The Hamiltonian is given as

$$\hat{H} = -\frac{\hbar^2}{2m_e}\sum_i \nabla_i^2 - \sum_{i,I}\frac{Z_l e^2}{|\mathbf{r}_i - \mathbf{R}_I|} + \frac{1}{2}\sum_{i\neq j}\frac{e^2}{|\mathbf{r}_i - \mathbf{r}_j|} - \frac{\hbar^2}{2}\sum_I \frac{1}{M_I}\nabla_I^2 + \frac{1}{2}\sum_{I\neq J}\frac{Z_I Z_J e^2}{|\mathbf{R}_I - \mathbf{R}_J|}, \tag{2.33}$$

where subscripts i, j represent electrons, and I, J represent the nuclei. This Hamiltonian includes the kinetic energy of both electron and nuclei, as well as the Coulomb interactions between electrons and electrons, nuclei and electrons, and between the nuclei. The use of the Born-Oppenheimer approximation [18] is essential when proceeding with the Hamiltonian (2.33). Here, the nuclei are treated as stationary, providing a static potential for the electrons. To justify this the main idea is that the nuclei are much more massive than the electrons, such that when the nuclei and electrons experience forces, the electrons will respond rapidly to any changes in the position of the nuclei, but the nuclei will essentially remain stationary when interacting with the electrons. The consequences of this allow for a more compact Hamiltonian,

$$\hat{H} = \hat{T} + \hat{V}_{\text{ext}} + \hat{V}_{\text{e-e}} + E_{\text{l-l}}. \tag{2.34}$$

Here, the first term is the kinetic energy operator for the electrons. The second is the interaction between the electrons and the stationary nuclei, and the third is the electron-electron interaction. The last term, $E_{\text{l-l}}$, now represents the nuclei-nuclei interaction, as well as all other energies that contribute to the total energy of the system but not to the description of the electrons. This term is regarded only as a simple classical additive term. It is this Hamiltonian which will be essential when analyzing the electronic structure.

The next step is to link the expectation value of the Hamiltonian to the electron density, where $\mathbf{r}_i$ represent spin and position for electron i. As such, the density operator is introduced,

$$\hat{n}(\mathbf{r}) = \sum_{i=1}^{N}\delta(\mathbf{r} - \mathbf{r}_i). \tag{2.35}$$

Introducing bra-ket notation, the particle density is given by the expectation value of $\hat{n}(\mathbf{r})$, where

the electron many-body wavefuntion is introduced as $\Psi(\mathbf{r}_1, \mathbf{r}_2 \cdots, \mathbf{r}_N)$,

$$n(\mathbf{r}) = \frac{\langle \Psi | \, \hat{n}(\mathbf{r}) \, | \Psi \rangle}{\langle \Psi | \Psi \rangle} = N \frac{\int \sum_{i=2}^{N} \mathrm{d}^3 r_i \sum_{\sigma_1} |\Psi|^2}{\int \sum_{i=1}^{N} \mathrm{d}^3 r_i |\Psi|^2}. \tag{2.36}$$

If the density does not obey $n^{\uparrow}(\mathbf{r}) = n^{\downarrow}(\mathbf{r}) = n(\mathbf{r})/2$, the density for each spin is obtained by excluding the sum over each spin configuration, σ_1. Likewise, the total energy is found by taking the expectation value of the Hamiltonian (2.34),

$$E = \langle \hat{T} \rangle + \langle \hat{V}_{\text{e-e}} \rangle + \int \mathrm{d}^3 r V_{\text{ext}}(\mathbf{r}) n(\mathbf{r}) + E_{\text{l-l}}. \tag{2.37}$$

Finding the eigenstates of the many-body Hamiltonian can be done by identifying the saddle points of (2.37), and the ground state wavefunction can be obtained by finding the minimum total energy with respect to all $\mathbf{r}_i$ in $\Psi(\mathbf{r}_1, \mathbf{r}_2 \cdots, \mathbf{r}_N)$. Even though the Born-Oppenheimer approximation is used, this is a very demanding task, especially when handling larger systems, as the systems have at least $3N$ variables in 3 dimensions. Thus, the stage is set for a theory which introduces a way to solve this problem, namely DFT.

2.4 Density functional theory

This section is mostly based on [10], and gives a short presentation of the basics of the DFT. The goal is to find properties of interacting many-particle systems, without doing the tedious ab initio method of solving the many-body Schrödinger equation directly. The proposed solution is surprisingly simple, namely that any property of the interacting system can be evaluated as a functional of the ground state density, which is local in the sense that it depends solely on the position. Theorems that claim such a density exists and the methods of solving the emerging equations are presented.

2.4.1 The Hohenberg-Kohn theorems

The main idea behind the approach of Hohenberg and Kohn is to incorporate a precise theory of many-body systems when formulating the DFT. This theory should apply to any interacting system of particles, and thus also to systems of electrons and fixed nuclei, such as systems with a Hamiltonian as presented in Equation (2.33). Two theorems summarize and set the starting point of DFT [19]. The two theorems could be stated as the following [10, p. 122].

- **Theorem 1:** "For any system of interacting particles in an external potential $V_{\text{ext}}(\mathbf{r})$, the potential $V_{\text{ext}}(\mathbf{r})$ is determined uniquely, except for a constant, by the ground state particle density $n_0(\mathbf{r})$."

- **Theorem 2:** "A *universal functional* for the energy $E[n]$ in terms of the density $n(\mathbf{r})$ can be defined, valid for any external potential $V_{\text{ext}}(\mathbf{r})$. For any particular $V_{\text{ext}}(\mathbf{r})$, the exact

ground state energy of the system is the global minimum value of this functional, and the density $n(\mathbf{r})$ that minimizes the functional is the exact ground state density $n_0(\mathbf{r})$."

Thus, finding the electron density which corresponds to the ground-state many-body wave equation should make it possible to obtain the exact properties of the system. This is due to the fact that all the properties of the system can be determined from the ground state electron density. This leads to the Hohenberg-Kohn definition of the energy as a functional,

$$E_{\mathrm{HK}}[n] = T[n] + E_{\mathrm{int}}[n] + \int \mathrm{d}^3 r V_{\mathrm{ext}}(\mathbf{r}) n(\mathbf{r}) + E_{\text{l-l}}. \tag{2.38}$$

Here $[n]$ is introduced, as to show that the energy is a functional[2] of the electron density. Also, the last term, $E_{\text{l-l}}$, is the nuclei interaction energy. This is the fundation for the Hohenberg-Kohn functional,

$$F_{\mathrm{HK}} = T[n] + E_{\mathrm{int}}[n]. \tag{2.39}$$

The kinetic and interaction energies of the electrons are functionals of the density, and this functional contains both the kinetic and the potential energies of the interacting electron system.

2.4.2 Constrained search formulation

The formalism developed by Levy and Lieb [20][21] provides an instructive definition of the functional. The ground state energy of the system can be found by starting with the many-body wavefunction and minimizing with respect to all variables present in the desired wavefunction, which can be a tedious task. Levy and Lieb introduced a concept where the class of many-body wavefunctions Ψ with the same density $n(\mathbf{r})$ is considered. The energy for any wavefunction can be expressed as

$$E = \langle \Psi | \hat{T} | \Psi \rangle + \langle \Psi | \hat{V}_{\text{e-e}} | \Psi \rangle + \int \mathrm{d}^3 r V_{\mathrm{ext}}(\mathbf{r}) n(\mathbf{r}) + E_{\text{l-l}}, \tag{2.40}$$

where the first term on the right-hand side is the kinetic energy of the electrons, the second is the electron-electron interaction energy, and the second to last term represents the interaction of the electron density with the external potential from the fixed nuclei. The last term is simply the remaining nucleus-nucleus interaction. The unique lowest energy for the density corresponding to the class of wavefunctions can be obtained by minimizing (2.40),

$$E_{LL}[n] = \min_{\Psi \to n(\mathbf{r})} [\langle \Psi | \hat{T} | \Psi \rangle + \langle \Psi | \hat{V}_{\text{e-e}} | \Psi \rangle] + \int \mathrm{d}^3 r V_{\mathrm{ext}}(\mathbf{r}) n(\mathbf{r}) \mathrm{d}^3 r + E_{\text{l-l}}. \tag{2.41}$$

[2]The importance of differentiating between a function and a functional becomes apparent when considering that a functional maps a space X to the real or complex numbers. A simple example of this is the integral where F is a functional of $g(x)$, $F[g] = \int_{x_1}^{x_2} \mathrm{d}x g(x)$

The definition of the Levy-Lieb functional of the density is then,

$$F_{LL}[n] = \min_{\Psi \to n(\mathbf{r})} [\langle \Psi | \hat{T} | \Psi \rangle + \langle \Psi | \hat{V}_{\text{e-e}} | \Psi \rangle]. \tag{2.42}$$

The functional (2.42) is so called "N-representable", meaning that for a wavefunction for N electrons with any $n(\mathbf{r})$ derivable from this wavefunction, the functional is defined. This representability is different from that of the Hohenberg-Kohn functional (2.39), which is "V-representable", meaning that the functional is only defined for $n(\mathbf{r})$ that are generated by some known external potential. For such a known external potential, at the minimum of the total energy of the system the Levy-Lieb functional is equal to the Hohenberg-Kohn functional, given by the fact that the minimum corresponds to a density that can be generated by the external potential. Regarding the electron density, there exists a few restrictions for the density that must be obeyed, but theses restrictions will not be discussed in detail. Given that this functional could be defined for any density, the exact density - as well as the energy of the system - can be found in theory.

2.4.3 The Kohn-Sham equations and the auxiliary system

The idea behind the Kohn-Sham approach is to omit the problematic interacting many-body system discussed in Subsection 2.3.2, by introducing a simpler auxiliary system. The concept involves doing calculations on a non-interacting system, representing the interacting system with the same ground state density. The independent particle equations should be possible to solve, and the many-body effects are represented in the exchange-correlation (xc) functional of the density. The Hamiltonian for the auxiliary system is given as

$$\hat{H}^{\sigma}_{\text{aux}} = -\frac{\hbar^2}{2m_e}\nabla^2 + V^{\sigma}(\mathbf{r}), \tag{2.43}$$

where $V^{\sigma}(\mathbf{r})$ represent a local potential acting on an electron of spin σ at position $\mathbf{r}$. The ground state satisfying this Hamiltonian have N^{σ} orbitals, denoted $\psi^{\sigma}_i(\mathbf{r})$. The kinetic energy and the density of the auxiliary system is given as a sum over spins and orbitals. These properties can be expressed as

$$T_s = \frac{1}{2}\sum_{\sigma}\sum_{i=1}^{N^{\sigma}} \int \mathrm{d}^3 r |\nabla \psi^{\sigma}_i(\mathbf{r})|^2, \tag{2.44}$$

and

$$n(\mathbf{r}) = \sum_{\sigma}\sum_{i=1}^{N^{\sigma}} |\psi^{\sigma}_i(\mathbf{r})|^2. \tag{2.45}$$

Here Hartree atomic units are introduced, $\hbar = m_e = e = 4\pi/\epsilon_0 = 1$. The concept of Kohn-Sham is to rewrite the ground state energy functional (2.38) as

$$E_{KS}[n] = T_s[n] + \int \mathrm{d}\mathbf{r} V_{\text{ext}}(\mathbf{r}) n(\mathbf{r}) + E_{\text{H}}[n] + E_{\text{l-l}} + E_{\text{xc}}[n]. \tag{2.46}$$

Here $E_{\text{l-l}}$ represents the nuclei-nuclei interaction, and $V_{\text{ext}}(\mathbf{r})$ is the external potential, from both the nuclei and external fields. The Hartree energy, $E_H[n]$, takes care of the Coloumb interaction the electron density has with itself,

$$E_{\text{H}}[n] = \frac{1}{2}\int \mathrm{d}^3 r \mathrm{d}^3 r' \frac{n(\mathbf{r})n(\mathbf{r}')}{|\mathbf{r}-\mathbf{r}'|}. \tag{2.47}$$

If the electron density is well defined, the remaining problem is $T_s[n]$ and $E_{xc}[n]$, which must be unique functionals of the density by the Hohenberg-Kohn theorems. By comparison of the Hohenberg-Kohn definition of the energy as a functional (2.38), since the density of the auxiliary system must be equal to the density of the interacting system, the xc energy can be expressed as

$$E_{\text{xc}}[n] = F_{\text{HK}} - T_{\text{s}}[n] - E_{\text{H}}[n] = \left\langle \hat{T} \right\rangle - T_{\text{s}}[n] + \left\langle \hat{V}_{e-e} \right\rangle - E_{\text{H}}[n]. \tag{2.48}$$

Here the expectation values of the operators are introduced, as $\left\langle \hat{T} \right\rangle = T[n]$, and $\left\langle \hat{V}_{e-e} \right\rangle = E_{\text{int}}[n]$, showing that $E_{\text{xc}}[n]$ is a functional. Equation (2.48) shows that the xc energy is the difference between the kinetic energy and the electron-electron interaction energy for the interacting many-body system and the auxiliary non-interacting system. Approximating $E_{\text{xc}}[n]$ is a major part of any DFT calculations, and its importance and some of its aspects will be discussed in Section 2.5.

Solving the equations for the ground state Kohn-Sham auxiliary system can be done by minimizing with respect to the particle density. Seen as E_{KS} is given as a functional, and T_s from Equation (2.44) and $n(\mathbf{r}) = \sum_\sigma n(\mathbf{r},\sigma)$ from Equation (2.45), are functionals of the orbitals, varying the wavefunctions leads to the variational equation. The orthonormalization constrains are

$$\left\langle \psi_j^\sigma \middle| \psi_i^{\sigma'} \right\rangle = \delta_{i,j}\delta_{\sigma,\sigma'}, \tag{2.49}$$

and the variational equation can be written as

$$\frac{\delta E_{KS}}{\delta \psi_i^{\sigma *}(\mathbf{r})} = \frac{\delta T_s}{\delta \psi_i^{\sigma *}(\mathbf{r})} + \left[\frac{\delta E_{\text{ext}}}{\delta n(\mathbf{r},\sigma)} + \frac{\delta E_{\text{H}}}{\delta n(\mathbf{r},\sigma)} + \frac{\delta E_{\text{xc}}}{\delta n(\mathbf{r},\sigma)}\right]\frac{\delta n(\mathbf{r},\sigma)}{\delta \psi_i^{\sigma *}(\mathbf{r})} = 0. \tag{2.50}$$

Introducing equations (2.44) and (2.45) for T_s and $n(\mathbf{r},\sigma)$ the Schrödinger-like eigenvalue equations with the Kohn-Sham effective Hamiltonian becomes

$$H_{KS}^\sigma \psi_i^\sigma(\mathbf{r}) = \left[-\frac{1}{2}\nabla^2 + V_{KS}^\sigma(\mathbf{r})\right]\psi_i^\sigma(\mathbf{r}) = \epsilon_i^\sigma \psi_i^\sigma(\mathbf{r}), \tag{2.51}$$

where the effective potential is

$$V_{KS}(\mathbf{r}) = V_{\text{ext}}(\mathbf{r}) + \frac{\delta E_{\text{H}}}{\delta n(\mathbf{r},\sigma)} + \frac{\delta E_{\text{xc}}}{\delta n(\mathbf{r},\sigma)} = V_{\text{ext}}(\mathbf{r}) + V_{\text{H}}(\mathbf{r}) + V_{\text{xc}}^\sigma(\mathbf{r}). \tag{2.52}$$

A self-consistent loop can be used to solve the Kohn-Sham equations. The start of this loop

consists of an initial guess of $n^{\uparrow}(\mathbf{r})$, $n^{\downarrow}(\mathbf{r})$, for which the loop must be carried out for each spin density. Note that this must be done simultaneously, as the potential for each density is a functional of the density of both spins. Then the effective potential is calculated, and Equation (2.51) can be solved. New spin densities are calculated by Equation (2.45), and a consistency check is done. If the new densities are self-consistent with the previously generated densities with an appropriately small error, it means that the ground state density has been obtained, and the minimization is done. If the densities are not self-consistent, a new potential is calculated and the process is repeated. Once the correct ground state densities are found, properties of the system can be extracted, as predicted by the Hohenberg-Kohn theorems. This approach has many advantageous features, as the Hartree energy and the kinetic energy of the non-interacting system are easy to calculate, and Equation (2.51) is easier to solve than the many-body interacting Schrödinger equation. Obtaining an approximation for $E_{\mathrm{xc}}[n]$ and thus also $V_{\mathrm{xc}}(\mathbf{r})$ is the motivation for the following section.

2.5 Approximations of the exchange-correlation functional

The main source of errors in DFT calculations is the approximation of the xc functional. If the functional were precisely known, the Kohn-Sham equations would give the exact answers for the electronic system. The approximations done are therefore essential for the correctness and precision of any properties gathered from the calculated electron density. In this section, the local spin density approximation (LSDA) and the generalized gradient approximation (GGA) are discussed. This section is based on [10].

2.5.1 Local spin density approximation

The simplest approximation for the xc functional, $E_{\mathrm{xc}}[n]$, is the local spin density approximation. This approximation is based on the presumption that the system and properties studied can be modelled as being close to that of the homogeneous electron gas [22], such that the exchange and correlation effects are considered to be only local. Therefore, the xc energy is a space integral, where the xc energy density is set to be the same as for the homogeneous electron gas with the same density. This results in the following expression for the xc energy,

$$E_{\mathrm{xc}}^{\mathrm{LSDA}}[n^{\uparrow}, n^{\downarrow}] = \int \mathrm{d}^3 r n(\mathbf{r}) \epsilon_{\mathrm{xc}}^{\mathrm{hom}}(n^{\uparrow}(\mathbf{r}), n^{\downarrow}(\mathbf{r})) \tag{2.53}$$

This equation assumes two collinear spin densities, $n^{\uparrow}(\mathbf{r})$ and $n^{\downarrow}(\mathbf{r})$, and $\epsilon_{\mathrm{xc}}^{\mathrm{hom}}$ is the known local xc energy density per particle of a homogeneous electron gas with the same density as the system analyzed. For cases where the system is unpolarized, the local density approximation (LDA) is simply found by setting $n^{\uparrow}(\mathbf{r}) = n^{\downarrow}(\mathbf{r}) = n(\mathbf{r})/2$, where $n(\mathbf{r})$ is the total density. The L(S)DA has its uses, but the approximation is not suited to handle systems where the self-interaction of the electron density is a crucial factor. As this xc energy functional (2.53) does not take into account

the local gradients of the electron density, more sophisticated approximations are often desired.

2.5.2 Generalized gradient approximation

The idea behind the GGA is to introduce a weight that depends on the gradients of the electron density. This weight can be used when constructing functionals superior to the LSDA, as the GGA does not solely depend on the xc energy density of a homogeneous electron gas with the same density as the studied system. The GGA xc energy functional can be defined as

$$E_{\mathrm{xc}}^{\mathrm{GGA}}[n^{\uparrow}, n^{\downarrow}] = \int \mathrm{d}^3 r n(\mathbf{r}) \epsilon_{\mathrm{xc}}(n^{\uparrow}, n^{\downarrow}, |\nabla n^{\uparrow}|, |\nabla n^{\downarrow}|, |\nabla^2 n^{\uparrow}|, |\nabla^2 n^{\downarrow}|, \cdots), \tag{2.54}$$

and also introducing the weight,

$$E_{\mathrm{xc}}^{\mathrm{GGA}}[n^{\uparrow}, n^{\downarrow}] = \int \mathrm{d}^3 r n(\mathbf{r}) \epsilon_{\mathrm{x}}^{\mathrm{hom}}(n) F_{\mathrm{xc}}(n^{\uparrow}, n^{\downarrow}, |\nabla n^{\uparrow}|, |\nabla n^{\downarrow}|, |\nabla^2 n^{\uparrow}|, |\nabla^2 n^{\downarrow}|, \cdots), \tag{2.55}$$

where $\epsilon_{\mathrm{x}}^{\mathrm{hom}}$ is the exchange part of the xc energy for the unpolarized homogeneous electron gas. It is possible to reduce Equation (2.55) into two parts, one containing the exchange part and one containing the correlation part. When this is done, the exchange parts, $E_{\mathrm{x}}^{\mathrm{GGA}}[n]$ and $F_x(n, |\nabla n|)$ are the same as for an spin-unpolarized system of density $n(\mathbf{r})$. It is common to work with the exchange part of the weight as $F_{\mathrm{x}}(s_i)$, where s_i is the i'th order reduced density gradient, defined as

$$s_i = \frac{|\nabla^i n|}{2^i (3\pi^2)^{i/3} n^{1+i/3}}, \tag{2.56}$$

such that the weighted exchange energy can be written as

$$E_{\mathrm{x}}^{\mathrm{GGA}}[n] = \int \mathrm{d}^3 r n(\mathbf{r}) \epsilon_{\mathrm{x}}^{\mathrm{hom}}(n) F_{\mathrm{x}}(s_i). \tag{2.57}$$

The correlation part of $E_{\mathrm{xc}}^{\mathrm{GGA}}[n^{\uparrow}, n^{\downarrow}] = E_{\mathrm{x}}^{\mathrm{GGA}}[n] + E_{\mathrm{c}}^{\mathrm{GGA}}[n^{\uparrow}, n^{\downarrow}]$ is much more complex than the exchange part. Its overall contribution to the xc energy is in some cases small but not in any way neglectable, compared to the contribution stemming from the exchange part. More discussion about the convergence of the correlation part with respect to s_i and the reduced density gradient expansion of the correlation weight can be found in [23] and [24].

2.6 Cluster expansion for alloy systems

In this section, theoretical framework for the CE method is presented to show the relation between the configurational energy of an alloy and the ECIs. The statistics behind the CE evaluation and a way of obtaining the ECIs with linear regression are also included.

2.6.1 Cluster expansion and the configurational energy

A binary alloy consisting of atoms of type A and B can be represented discretely by a configurational variable σ. At a given lattice point $\sigma = \pm 1$, depending on whether the point is occupied by an atom of type A or B. A point cluster with one lattice point has a one dimensional configurational space associated with it, and the scalar product of two functions in this space, $f(\sigma)$ and $g(\sigma)$, is defined as [6]

$$\langle f, g \rangle = \frac{1}{2\cosh(\mu)} \sum_{\sigma=\pm 1} e^{\mu\sigma} f(\sigma) g(\sigma), \tag{2.58}$$

where μ is a constant. Given a value of μ, the one-dimensional configuration space spanned by σ has a complete and orthonormal basis given by two polynomials. Setting $\mu = 0$, the two polynomials of order 0 and 1 are expressed as

$$\phi_0(\sigma) = 1, \quad \phi_1(\sigma) = \sigma. \tag{2.59}$$

This basis is for the point cluster, but the orthogonal basis can be expanded to any finite cluster or the whole crystal of N lattice sites, given the initial polynomials for the point cluster. Such a finite cluster can be defined as

$$\alpha = \{p_1, p_2, \ldots, p_{n_\alpha}\}, \tag{2.60}$$

where p_i represents point i in the cluster α containing n_α cluster sites. The configurational space representing this cluster is given by the product of the subspaces at each site in α, and can now be expressed as an n_α-dimensional vector,

$$\boldsymbol{\sigma} = \{\sigma_1, \sigma_2, \ldots, \sigma_{n_\alpha}\}. \tag{2.61}$$

An orthonormal basis for the cluster α in the space spanned by this discrete vector is given by the functions $\Phi_\alpha(\boldsymbol{\sigma}_\alpha)$, and is constructed by all possible products of the two polynomials from Equation (2.59),

$$\Phi_\alpha(\boldsymbol{\sigma}_\alpha) = \prod_{i \in \alpha} \phi_1(\sigma_i). \tag{2.62}$$

This function is called the characteristic function of the cluster α, and as the polynomials from Equation (2.59) are inherently orthonogal so is $\Phi_\alpha(\boldsymbol{\sigma}_\alpha)$. Given that α and β are subclusters of cluster γ the orthogonality of the characteristic functions is expressed as

$$\langle \Phi_\alpha, \Phi_\beta \rangle = \frac{1}{2^{n_\gamma}} \sum_{\sigma_1=\pm 1} \cdots \sum_{\sigma_n=\pm 1} \Phi_\alpha(\boldsymbol{\sigma}_\alpha) \Phi_\beta(\boldsymbol{\sigma}_\beta) = \delta_{\alpha,\beta}, \tag{2.63}$$

where $\delta_{\alpha,\beta}$ is the Kronecker delta. The scalar product between two functions $f(\sigma_\gamma)$ and $g(\sigma_\gamma)$,

equivalent to Equation (2.58), in the configurational space of cluster γ is defined by

$$\langle f, g \rangle = \frac{1}{2^{n_\gamma}} \sum_{\sigma_1=\pm 1} \cdots \sum_{\sigma_n=\pm 1} f(\boldsymbol{\sigma}_\gamma) g(\boldsymbol{\sigma}_\gamma). \tag{2.64}$$

By using the orthonormal basis, $\Phi_\alpha(\boldsymbol{\sigma})$, it is possible to expand a function dependent on the configuration $\boldsymbol{\sigma}$ of cluster α using the ECIs defined as the scalar product,

$$V_\alpha = \langle \Phi_\alpha(\boldsymbol{\sigma}), E \rangle, \tag{2.65}$$

where E is the energy. Expanding the configurational energy as a sum, using the ECIs and the orthonormal basis yields

$$E(\boldsymbol{\sigma}) = \sum_\alpha V_\alpha \Phi_\alpha(\boldsymbol{\sigma}). \tag{2.66}$$

Having introduced the complete and orthogonal basis in the configurational space of the clusters, system properties can be expressed through the CE by the use of the ECIs. The main challenge of the construction of a CE model is thus to find clusters that map the configuration to the desired physical quantity with a proper degree of precision.

2.6.2 Cross-validation score and errors in CE models

In practice, only a finite number of ECIs can be used when mapping the configurational space to a physical quantity, even though, theoretically, an infinite number of unknowns exists. If too few terms are used, the truncated CE could fail to predict all sources of energy fluctuations, and if too many terms are kept, overfitting could occur. The mean-squared-error of the predicted energies for structures included in the CE model could be small, especially if similar structures are used to develop the CE model. A small mean-square-error is not in itself a proof that the model is accurate, as the model could fail to accurately predict properties of structures differing to a large degree from those included in the initial data set used for training the CE. For evaluating a CE model, the cross-validation (CV) score of the model can be examined, by comparing the energy of a structure found by DFT with the energy of the structure predicted by the CE model [25]. The CV score can be expressed as

$$CV = \frac{1}{n} \sum_{i=1}^{n} (E_i - \hat{E}_i)^2, \tag{2.67}$$

where n is the total number of structures, E_i is the energy of structure i found by DFT calculations, and $\hat{E}_i$ is the energy of structure i predicted by a fit to the energies of all the structures included in the training set, excluding structure i. The CV score can hide some information about the power of the model, as it is an average value. If the energy of one of the n structures is predicted with much larger error than other structures, the residual of this energy prediction will be large compared to the residuals of the other energy predictions, as the residual of the

predicted energy of structure i is defined as

$$e_i = E_i - E_i^p, \tag{2.68}$$

where E_i is as above the energy of structure i calculated by DFT, and E_i^p is the energy predicted for structure i by a fit to the energies of all the structures, including structure i. In the same way, the leave-one-out residual can be defined similarly to Equation (2.68), where the leave-one-out residual is the difference between the DFT energy and the energy predicted by a fit to the energies of all the structures, excluding structure i. Thus, by examining the residuals statistical outliers can be identified. The square of the residuals of the energy predictions for the set of n structures can be used to calculate the root-mean-square error (RMSE) of the CE model,

$$RMSE = \left(\frac{1}{n} \sum_{i=1}^{n} e_i^2 \right)^{1/2}. \tag{2.69}$$

2.6.3 Selection of the ECIs

For fitting the ECIs to the energy of the different configurations, linear regression is used. Some regression methods are better suited for handling the DFT calculated energies, but a theme for the methods used is that they need to take overfitting into account. This is due to the selection of the ECIs, since there are many possible clusters to choose from. Therefore it is often regression methods that set some ECIs to zero that gives the best predictive power. If $\mathbf{w}$ is an $N \times 1$ signal where most of the coefficients are zero, the system can be expressed as [26]

$$\mathbf{y} = \Phi \mathbf{w} + \mathbf{n}. \tag{2.70}$$

Here, $\mathbf{y}$ is $M \times 1$ linear measurements of the unknown signal $\mathbf{w}$, and $\mathbf{n}$ is the acquisition noise. For the case of fitting to the DFT energies, $\mathbf{w}$ represents the ECI. The measurements, $\mathbf{y}$, are taken with a measurement matrix Φ,

$$\Phi = [\phi_1, \phi_2, \cdots, \phi_N], \tag{2.71}$$

of size $N \times M$ with $M \ll N$. The original signal $\mathbf{w}$ can be in some cases be reconstructed accurately by a reconstruction algorithm when the number of measurements is less than the number of coefficients, given mathematically by the condition $M \ll N$. This is according to the theory of compressive sensing [27]. Utilizing the sparsity of $\mathbf{w}$ the reconstruction algorithm can be expressed by restricting the l^p norm of w, where the l^p norm of $\mathbf{w}$ is defined as

$$||\mathbf{w}||_p = (|w_1|^p + |w_2|^p + \cdots + |w_N|^p)^{1/p}. \tag{2.72}$$

The constraint set upon $||\mathbf{w}||_p$ is $0 \leq p \leq 1$, and the resulting reconstruction algorithm can be

formulated as

$$\hat{\mathbf{w}} = \underset{\mathbf{w}}{\operatorname{argmin}}\{||\mathbf{y} - \Phi\mathbf{w}||_2^2 + \tau||\mathbf{w}||_p\}, \tag{2.73}$$

where τ is introduced as a regularization constant. In the Bayesian approach, all unknowns are assumed to be stochastic quantities which are associated with certain probability distributions. The motivation behind introducing priors in Bayesian statistics is that in some cases properties of the input signal can be assumed, giving the algorithm extra information about the system studied. For obtaining the ECIs, priors can be utilized to take into account information about the physical system when doing calculations. The Bayesian compressive sensing method utilizes a Laplace prior with the unknown coefficients of $\mathbf{w}$ to model the sparsity of the signal, and creates an iterative algorithm for finding the ECIs which reproduce the calculated DFT energies. How the priors are introduced in the model and the restrictions set on the probability distributions are further discussed in [26].

2.7 Monte Carlo methods and simulations

When doing calculations with DFT the energies are extrapolated to 0 K, making it difficult to obtain any thermodynamic properties for the systems studied. Also, the systems have to be relatively small when doing DFT calculations, limiting the structural properties which are possible to calculate. Using MC methods, atomic systems can be analyzed at any given temperature, and the size of the structures can be expanded to include more than 1000 atoms [28, p. 165]. Here, doing MC simulations in the canonical and the semi-grand canonical ensemble is discussed, with a focus on binary alloy systems. The main references for this section is [11], [28] and [29].

2.7.1 Monte Carlo simulations in the canonical ensemble

For a system containing N particles, the canonical ensemble is a statistical collection containing all possible microstates of the system. For a binary alloy, the microstates in the ensemble correspond to all configurations possible to construct at a given concentration. Some parameters restrict the behaviour of the system, as it has a fixed concentration and volume as well as a fixed total number of particles. The system is surrounded by a heat bath with temperature T, which it is in thermal equilibrium with. It is therefore the temperature that determines the statistical properties of the system, such energy fluctuations as well as the probability distribution determining the occupation of the different microstates.

When doing MC simulations in the canonical ensemble, the number of possible configurations in a binary alloy with respect to which atoms are located at which sites becomes large, even if the atomic concentration is kept constant. The MC methods are advantageous as they are constructed in such a way that the configurations with greatest statistical importance are those extracted from the possible configurations. Using MC methods, equilibrium states, thermodynamic properties

and ground states can be identified. Let the configurational space of a binary alloy be defined as in Equation (2.61), and choose a random configuration of atoms at a given concentration as a starting point. The total number of atoms in the structure must be kept constant. For a given temperature, T, N_{MC} MC steps are performed. The first part of a MC step consists of randomly swapping two atoms of different types. If $\boldsymbol{v}$ is the configuration of atoms,

$$\boldsymbol{v} = \{\dots, 1, -1, 1, 1, -1, -1, \dots\}, \tag{2.74}$$

a new configuration, $\boldsymbol{v'}$, could be illustrated as

$$\boldsymbol{v'} = \{\dots, 1, -1, -1, 1, 1, -1, \dots\}, \tag{2.75}$$

where two randomly picked atoms of different types A and B have been swapped. The next step is to evaluate the energy difference between the two configurations, using the expression for the configurational energy from Equation (2.66) which can be obtained by using the ECI for the binary system obtained through the CE. The energy difference is expressed as

$$\Delta E = E(\boldsymbol{v'}) - E(\boldsymbol{v}), \tag{2.76}$$

which is negative if the new configuration, $\boldsymbol{v'}$, is energetically favorable compared to $\boldsymbol{v}$. The temperature dependence is introduced through the Boltzmann distribution, which is included in the probability of accepting the new state. The Metropolis-Hastings algorithm [29] is a commonly used algorithm that uses such a temperature-dependent selection method. The selection probability used in this algorithm is expressed as

$$\min(1, \exp(-\frac{\Delta E}{k_{\mathrm{B}}T})), \tag{2.77}$$

and the process is repeated for the configuration $\boldsymbol{v}$ or $\boldsymbol{v'}$, depending on which one is picked. Choosing the number of MC steps to be performed can depend on which properties of the system is sought after. One choice is to let N_{MC} depend on the number of atoms and the concentration of the system, as the number of possible microstates of the system is dependent on these properties. Another possibility is to equilibriate the system with an unknown N_{MC}, but terminating the process when the variance of the energy between states has reached a given value. When a near-ground or ground state is obtained, thermodynamic properties can be extracted, and the path of atomic configurations chosen by the algorithm can be traced.

2.7.2 Monte Carlo simulations in the semi-grand canonical ensemble

The semi-grand canonical ensemble is constructed in much the same way as the canonical ensemble. This ensemble can be though of as a mixture of the canonical and the grand-canonical ensemble, which in the latter both the concentration as well as the total number of particles can vary. In the semi-grand canonical ensemble, while the concentration is allowed to vary, the total number of particles is fixed. Also, the temperature and the chemical potential are fixed, while the total energy of the system is allowed to fluctuate.

When doing MC simulations in this ensemble, the selection method for selecting a new state can be done as in the canonical ensemble, using Equation (2.77), but the way of constructing new configurations is different. Instead of swapping two atoms of different types, a random site in the structure is selected, and the atom type at this site is swapped. Analogous to the configurations in the canonical ensemble, equations (2.78) and (2.79), the configurations in the semi-grand canonical ensemble can be defined in the configurational space as

$$\boldsymbol{v} = \{\dots, 1, -1, 1, 1, -1, -1, \dots\}, \tag{2.78}$$

and a new configuration can be illustrated as

$$\boldsymbol{v'} = \{\dots, 1, -1, 1, 1, 1, -1, \dots\}, \tag{2.79}$$

where one atom have been replaced by an atom of the other type. This changes the chemical composition of the system and allows for energy fluctuations. The temperature, T, and the chemical potential, μ, are therefore externally imposed parameters determining the statistical properties of the system.

2.7.3 Phase boundary tracing

A phase diagram for a binary alloy is often used to determine macroscopic and microscopic material properties at different compositions and temperatures. MC simulations can be used to trace phase boundaries, and thus used to identify regions where first-order phase transitions occur, as well as regions containing stable phases. A thermodynamic potential per atom for a system in the semi-grand canonical ensemble can be expressed using the partition function as [30]

$$\phi(\beta, \mu) = -\frac{1}{\beta N} \ln\left(\sum_i \exp(-\beta N(E_i - \mu x_i))\right). \tag{2.80}$$

Here, N is the fixed total number of particles in the system, E_i is the internal energy per atom for state i, x_i is the concentration of state i and $\beta = 1/(k_B T)$, where k_B is Boltmann's constant, and T is the temperature. μ is referred to as the chemical potential, or rather the difference in the chemical potential for the two atoms types A and B, $\mu = \mu_A - \mu_B$. The thermodynamic

potential can also be expressed as a differential,

$$\mathrm{d}(\beta\phi) = (E - \mu x)\mathrm{d}\beta - \beta x \mathrm{d}\mu, \tag{2.81}$$

where E is the systems average energy, and x is the average concentration. This differential equation allows for finding the thermodynamic potential through integration,

$$\phi(\beta_1, \mu_1) = \frac{\beta_0}{\beta_1}\phi(\beta_0, \mu_0) + \frac{1}{\beta_1}\int_{(\beta_0,\mu_0)}^{(\beta_1,\mu_1)} (\mathrm{d}\beta(E - \mu x) - \mathrm{d}\mu\beta x). \tag{2.82}$$

If MC simulations are done with constant μ, Equation (2.82) reduces to

$$\phi(\beta_1, \mu) = \frac{\beta_0}{\beta_1}\phi(\beta_0, \mu) + \frac{1}{\beta_1}\int_{\beta_0}^{\beta_1} \mathrm{d}\beta(E - \mu x), \tag{2.83}$$

where the integral can be solved numerically along a path in β which does not cross a phase transition. This way, MC simulations in the semi-grand canonical ensemble can calculate E and x for a given β and μ.

Identifying $\phi(\beta_0, \mu)$ in the low temperature limit can be done through the definition of the thermodynamic potential with the partition function. Defining $\tilde{E}_i = E_i - \mu x_i$ and $\tilde{E}_0$ as the energy in the low temperature limit, Equation (2.80) can be written as

$$\exp(-\beta\phi) = \sum_i \exp(-\beta\tilde{E}_i)\exp(-\beta\tilde{E}_0)\exp(\beta\tilde{E}_0). \tag{2.84}$$

This equation can again be rewritten by taking the logarithm on both sides, changing signs and dividing by β,

$$\phi = \tilde{E}_0 - k_B T \ln\left(\sum_i \exp\left(-\frac{\tilde{E}_i - \tilde{E}_0}{k_B T}\right)\right). \tag{2.85}$$

As $\tilde{E}_i \geq \tilde{E}_0$, it is clear that $\lim_{T\to 0}\phi = \tilde{E}_0$, making it possible to calculate the first term in Equation (2.83).

When calculating the thermodynamic potential. it is computationally advantageous to trace the phase boundaries, instead of calculating the potential in the entire region where a phase is stable. At one such boundary, there should exist β and μ such that a phase-separated mixture between phases α and γ are stable. At this point the condition $\beta\phi^\alpha = \beta\phi^\gamma$ must be true. When the total differential of this equation is taken, the result can be written as

$$\frac{\mathrm{d}\mu}{\mathrm{d}\beta} = \frac{E^\gamma - E^\alpha}{\beta(x^\gamma - x^\alpha)} - \frac{\mu}{\beta}. \tag{2.86}$$

Here E^γ and E^α are the energy for phase α and γ, while x^γ and x^α is the thermal average singlet correlation function for phase γ and α [7]. Requiring $\dfrac{d\mu}{d\beta} = 0$ at $T = 0$ gives the initial conditions

of Equation (2.86),

$$\mu(T=0) = \left[\frac{E^{\gamma} - E^{\alpha}}{(x^{\gamma} - x^{\alpha})}\right]_{T=0}. \tag{2.87}$$

Here energies for the two phases calculated by DFT can be used to locate a starting point when searching for μ and β for tracing the phase boundaries.

3 Computational methods

This chapter briefly explains the background of the computational methods used later on. The most relevant aspects of the chosen software for doing DFT calculations as well as user input data are discussed. The method of training the CE model from DFT data is presented. Lastly, computational details about the MC algorithm used is included, as well as discussion about doing calculations in different statistical ensembles.

3.1 DFT calculations

The use of DFT calculations for simulating atomic-scale systems such as molecules and atoms has increased vastly in recent years, and the evolution of both the theoretical ideas as well as the computational methods have accumulated to the modern DFT implementations used today [5]. As more powerful computers and data-centers have emerged, with greater core counts, bandwidth and memory, several research communities have embraced precise parallelized DFT codes such as GPAW [31][32][33] and VASP [34] in conjunction with simulation environments as the atomic simulation environment (ASE) [35], to understand more about the fundamental properties of materials.

3.1.1 GPAW

GPAW is a program package for doing electron structure calculations, using the projector augmented wave (PAW) method for numerical approximations. It is written in Python and C languages and can be used as a calculator with ASE objects. The 90/10 rule within computer science states that approximately 90% of the time spent running a program is used within 10% of the code. Therefore, even though most of the GPAW code is written in Python, the time consuming linear algebra and matrix operation functions used are written in C and uses several C-extensions from BLAS [36] and ScaLAPACK [37] to speed up performance. The reason for using C to improve the performance of the calculations is due to C often being faster than Python when doing numerical calculations [38]. The GPAW code is also highly parallelized by using the message passing interface (MPI) [39, p. 83], which is a huge advantage, especially when running simulations on supercomputers or large computer clusters. For these reasons GPAW can in certain cases reach close to 25% peak floating point performance, and do calculations on large data sets, even though parts of the code scale as $\mathcal{O}(N^2)$ and $\mathcal{O}(N^3)$ [40], where N is the input data size.

Using GPAW as a calculator in conjunction with an ASE Atoms object, the many functionalities of GPAW need to be taken into account. Different parameters are given to the GPAW calculator, specifying different limits and aspects of the calculations being done. The following discussion handles the most relevant GPAW input parameters for the calculations done later.

When choosing which mode used in the GPAW calculator, the choice is between expanding the wave functions in a real space grid, in a basis-set from atomic orbitals or as plane waves.

The calculations done in this project are done in reciprocal space, so the wave functions are expanded as plane waves. One of the reasons this expansion is used is because of the efficient way of calculating the stress tensors of the system in reciprocal space. The plane wave approach is also beneficial for doing calculations with smaller systems with a given periodicity, as the code implemented in GPAW for plane wave expansion parallelizes well. When using the plane wave approach one can specify the plane wave cutoff, E_c. This parameter is set as a boundary for the waves, such that only plane waves with energies $|\mathbf{k}+\mathbf{G}|^2/2 < E_c$ are allowed, where $\mathbf{k}$ is the wave vector and $\mathbf{G}$ is the reciprocal translation vector.

There is also an option for choosing how many bands are included for each spin. When doing calculations on metals, it can be beneficial to include several unoccupied bands for proper convergence.

The Brillouin-zone sampling is also taken care of in the GPAW calculator. The default sampling is with the Γ-point, and specifying the number of k-points, or the k-point density (points per Å^{-1}) is essential for stable DFT calculations. The k-point density is defined as

$$k_{\text{dens}} = N\frac{L}{2\pi}, \tag{3.1}$$

where N is the number of k-points, and L is the length of the unit cell along the corresponding reciprocal lattice vector. A Monkhorst-Pack sampling [41] can be used when specifying the number of k-points in each of the three directions of the reciprocal space is desired. It is also important to note the dependency of the number of k-points required for a given system volume. Due to the inverse nature of the Fourier Transform, i.e., $\text{m} \rightarrow \text{m}^{-1}$, small systems require more k-points than large systems to keep the k-point density roughly the same across the different sized systems.

GPAW also allows for controlling the smearing of the occupation numbers of the system. This parameter is set as k_BT in Equation (2.11), in units of eV, and the energies are extrapolated to 0 K afterward. For metals, the smearing around the calculated Fermi Level is useful, since occupancies near the Fermi Level can be between 0 and 1, due to the metals having partially filled bands [8, p. 162].

Lastly is choosing an appropriate xc functional. Different xc functionals are possible to choose from, as GPAW can use the xc functionals from libxc [42]. Both local density, generalized gradient, and hybrid density approximations are available. The simplest functional used in later calculations is the LDA [43][44]. This functional gives reasonable results for some systems, but for metals as researched in this work, a commonly used functional is the Perdew-Burke-Ernzerhof (PBE) xc functional [24]. This is a GGA functional, which is suitable, as it takes into consideration the large gradients of the electron density which often occurs in metals. The PBE functional is first order in the reduced density gradient s_i from Equation (2.56), so its weight depends both on the density and the first order derivative of the density.

3.1.2 The atomic simulation environment

ASE is used for handling the initialization of several simulation settings, such as geometry, cell size, and the organization of the atoms. This simulation environment provides many functionalities such as tools for constructing bcc and fcc cells, setting the desired system size and lattice constants as well as defining the boundary conditions of the system. The ASE Atoms objects can be viewed for controlling the crystal structure. Some of the initialized values used with ASE can decrease the run time of other tasks done with the joined ASE Atoms object and the GPAW calculator. The initial lattice constant and the initial magnetic moment for spin-polarized calculations should be set close to the expected values of the system, as less computer resources are used for the relaxation of the lattice as well as the convergence of the magnetic moment. The ASE database is also convenient, as e.g., Atoms objects, initial parameters, and GPAW input parameters can be stored properly for later use.

3.1.3 Local structure optimization

When doing calculations with atomic systems generated by ASE, it is often beneficial to optimize the atomic structures. The goal of the optimization algorithms is to scout the potential energy of the system, trying to find local saddle points. By moving the atoms around, e.g., by changing the lattice constants, the cell or the atomic positions, the algorithm tries to reduce the force on each individual atom such that the maximal force the atom is subjected to is less than some $f_{\max}$. In the following work, the preconditioned LBFGS algorithm and the BFGS algorithm are used [45]. The algorithms use the force returned by the calculator object, as well as the Hessian matrix of second derivatives with respect to atom positions, $\partial^2 E/(\partial x_i \partial x_j)$, to decide where to move the atoms in the next step. The LBFGS algorithm updates the inverse of the Hessian, and some approximations such as initial guesses for the Hessian are used to save computer resources. The LBFGS is used in conjunction with a sparse precondition algorithm, which helps with accelerating the geometry optimization and the identification of the local energy minima [46].

3.2 Development of the CE model

Here, details about the software used for doing CE with obtained DFT data and evaluating the results are discussed. The CE implementation used in this thesis is CLEASE [47], which is integrated with ASE. Theoretical aspects of the CE method and the statistical evaluation of the ECIs were discussed in Section 2.6.

3.2.1 Obtaining ECIs with CLEASE

When preparing structures for use in the CE model, it is crucial to select structures that cover most of the possible configurational space. To accomplish this, structures with atoms in random positions, covering the desired concentrations could be used. The simplest way of doing this is to

start with doing DFT calculations for small structures, evaluating the CV score, and increasing the size of the structures if all atom configurations for a given size are included in the model. Finding a set of small structures that through CLEASE provide a satisfying CV score and RMSE error is beneficial since it could save computer resources doing DFT calculations for the smallest structures possible. CLEASE accepts structures of any size, with both cubic and conventional unit cells. When preparing structures of different sizes, it is advantageous to check for symmetry equivalence between structures, as to avoid spending computer resources on doing DFT calculations on equivalent structures. ASE has this functionality for evaluating the symmetry between Atoms objects.

When evaluating the CE model and the ECIs it has produced, the convex hull [48] based on the CE predicted energies and the DFT energies could be examined. Structures on the convex hull could be near-ground or ground states, and it is paramount for further analysis that the CE model predicts the energies of these structures to a high degree of precision.

Some tuning of the regression is allowed, to minimize the CV score and to create ECIs which better predict the physical properties of the system. The noise, $\mathbf{n}$, from Equation (2.70) can be used to affect the linear regression as it enters in the first iteration of the algorithm. Also, an upper threshold for how far away the atoms in the ECIs can be distance wise, and an upper threshold for the number of atoms included in the ECIs can be used. These parameters allow for controlling the algorithm in such a way that the ECIs produced are not based on self-interaction between atoms due to the periodic boundary conditions employed in the calculations. Also, τ, in the reconstruction algorithm (2.73) can be used to regularize the CE evaluation method.

3.3 Monte Carlo simulations

When the ECIs for the atomic system studied are obtained through the CE, the ECIs can be used with MC simulations to expand the analysis further, as discussed in Section 2.7. In this thesis, a Markov chain MC simulation code developed by David Kleiven [49], based on the Metropolis-Hastings algorithm [29] is used. Here, details about the software are elaborated, and aspects of how it is used in this thesis are discussed.

3.3.1 Aspects of the Monte Carlo code

Several input parameters can be used to tune the MC code, such that the desired physical properties can be examined. The algorithm uses the ECIs obtained through the CE to calculate the energy of the system. It is therefore paramount that the CE model predicts the correct ground states of the system for the MC code to converge and obtain states which are representative of the physical system.

When initializing the system, the size of the system, the elements to include, their concentrations and the lattice structure are given as input parameters. The number of MC steps done at a given temperature, N_{MC}, is an important input parameter when doing simulations in all en-

sembles. When sampling different configurations, it is essential that a large enough sample space is checked to obtain the near lowest or lowest energy states. For this reason, systems with high amounts of possible configurations require higher N_{MC} to obtain representable physical results.

When doing simulated annealing in the canonical ensemble, a random alloy configuration restricted by the input parameters is created. For obtaining the near-ground or ground states of a system, the simulation starts at a high temperature and performs N_{MC} MC steps, before the temperature is decreased and a new series of MC steps are performed. The configurational energy of the system at different temperatures can be obtained, and thermodynamic properties such as the heat capacity (2.25) can be calculated. This method of annealing also allows for obtaining ground states at different atomic concentrations.

It is also possible to start from a non-random configuration, e.g., a known ground state, and increase the temperature through the MC simulations. These simulations can be done in both the canonical ensemble and the semi-grand canonical ensemble, depending on whether the atomic concentration should be allowed to vary. This simulates, among other things, the dissolution of the atoms as the thermal fluctuations are introduced.

The MC code has utilities that can be attached to the MC process when doing calculations. The trajectories of atoms in the system at different temperatures can be recorded, such that the movement of the atoms can be analyzed. From the tracing of the atoms in the canonical ensemble, the site order parameter can be obtained. The site order parameter (SOP) is defined as the number of atoms in the system which have moved positions one or more times due to thermal fluctuations. Thus, for a system of Z atoms, the SOP is 0 for a system at 0 K, and the maximum value is Z if all atoms have changed their initial positions. The reason for the SOP being a precise quantity for studying the behavior of the system at different temperatures lies in the systems desire to reduce its energy. Swapping two different types of atoms is the only possible way to alter the energy of the system in terms of the configuration in the canonical ensemble, as in this ensemble the atomic concentrations are kept constant.

3.3.2 Creating a domain of iron and silicon

This subsection explains how structures used later in MC simulations are constructed. The results are found in Subsection 4.5.2, where two phases are studied. The Fe_3Si structure is used to illustrate the setup for the calculations, as they are done in the same way for the FeSi system. The systems are constructed as a cube of bcc iron containing an empty volume inside shaped as a cube or an octahedron. This vacant volume is then filled with Fe_3Si such that the entire structure is dense. The cube of Fe_3Si is constructed the same way as in Figure 4.15a, and an example of an octahedron structure is shown in Figure 3.1a. The octahedron is created in such a way that the (111) planes of the bcc structure are exposed, as illustrated in Figure 3.1b. It is important to note that the octahedron does not solely contain repetitions of Fe_3Si structures. The smallest structure able to recreate the ordering of atoms in the Fe_3Si structure contains 16 atoms, such

that the octahedron shape can be considered a mapping of atom types from a cube of Fe_3Si to the shape of an octahedron.

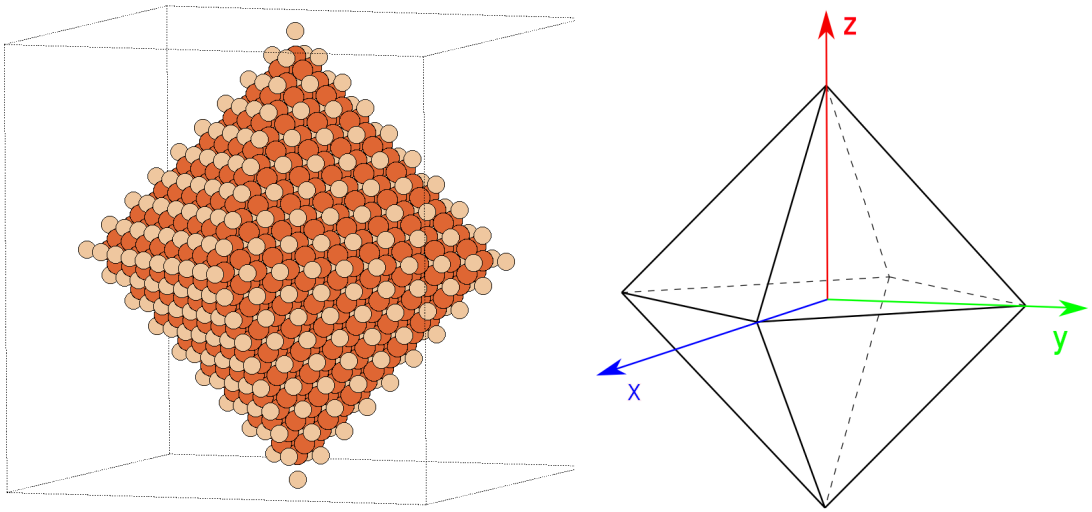

(a) Illustration of the Fe_3Si octahedron.

(b) Illustration of how the octahedron is constructed with respect to the axis.

Figure 3.1: Illustrations of the octahedron and its symmetries.

Illustrations of the Fe_3Si cube and octahedron situated inside the iron cube can be seen in Figure 3.2a and Figure 3.2b respectively. The structures are shown sliced in half, revealing the structure in the interior of the iron box. For the FeSi cube and the octahedron, the setup is the same, except that the configuration of the atoms in the interior cube and octahedron are such as illustrated in Figure 4.15b.

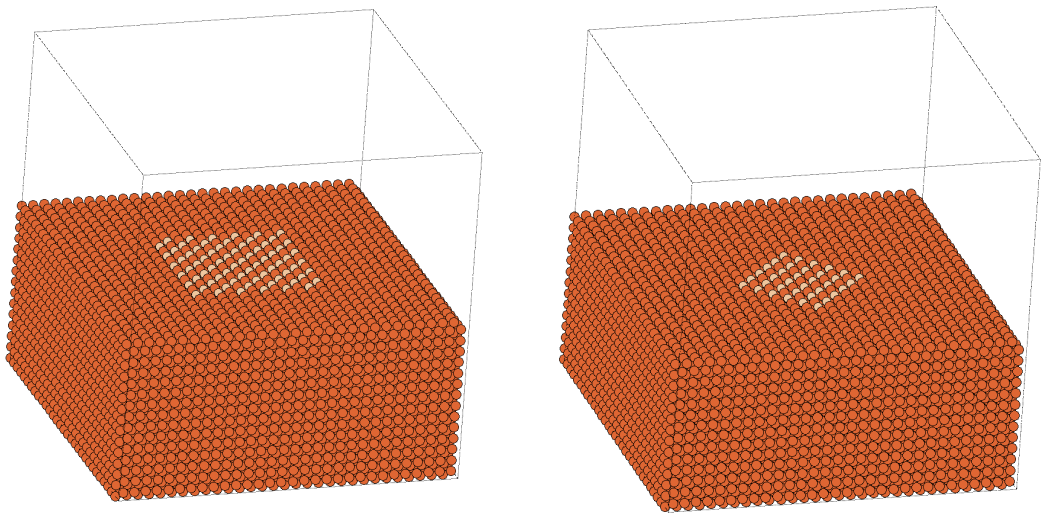

(a) Fe_3Si cube inside.

(b) Fe_3Si octahedron inside.

Figure 3.2: Illustrations of a Fe_3Si cube and an octahedron situated inside a larger iron encasement. The structures are shown sliced in half.

4 Results and discussion

This chapter contains presentations of the results in this thesis, as well as discussion. Comparison with other works is done when appropriate, and relevant theory is linked to the results. Firstly, the convergence of energy calculations is presented to study how total energy calculations depend on the GPAW input parameters. Following this, the magnetic moments for iron and iron-silicon alloys and the electronic band structure for iron and silicon are calculated with DFT. Then follows a presentation of the development of a CE model for a bcc iron-silicon alloy. The results obtained when doing simulated annealing and heating with MC based on the ECIs obtained from the CE are then presented. Lastly, phase boundary tracing is done for the iron-silicon system, and the surface energy associated with an interface between Fe_3Si and iron is investigated.

4.1 Energy convergence and GPAW input parameters

To obtain appropriate numerical values for the GPAW input parameters discussed in Section 3.1.1, a series of total energy convergence tests are done for bcc iron. The tests consist of doing energy calculations for the system, keeping all input parameters fixed except for one, which is varied over a suitable range. As DFT calculations take time and computer resources, it is wise to find parameters that give stable results as well as diminish the time used for computationally expensive tasks. The time needed to do a calculation is not only dependent on the system size, but also the numerical value of such parameters as the number of k-points and the energy cutoff. The following convergence tests for different parameters are all done by energy calculations, where the energy per atom for the systems are obtained, keeping all but one parameter fixed. If the varying parameter is h and the increment is h', convergence is obtained when $|E(h + h') - E(h)| < c$, where E is the energy per atom, and c is a constant which determines the level of convergence. Calculations on different system sizes might require different values of $h + h'$ before they are seen as converged. Therefore, it is common to do convergence tests when doing calculations with an unfamiliar system. It should be noted that the value of c is not specified by any literature, and is solely dependent on the specific system and which calculations are needed to be done. The fixed parameters used for the following energy calculations for iron systems of 1 atom and 64 atoms are listed in Table 4.1, and periodic boundary conditions are used throughout to represent the bulk. The structures are not relaxed with respect to the lattice, but the magnetic moment per atom is allowed to relax to its equilibrium value. The calculations are done this way since the two different sized structures could relax to different magnetic moments per atom.

Table 4.1: Fixed GPAW input parameters for the 1 and 64 atom iron systems.

	k-points	E_{cut} [eV]	$k_{\text{B}}T$ [eV]	nbands
1 atom	343	500	0.05	-5
64 atoms	27	700	0.05	-8

The first parameter studied is the number of k-points. In reciprocal space, the k-points form a cube in 3 dimensions, such that the total number of k-points is evenly distributed in all three directions. Figure 4.1 shows that for the one atom system the changes in energy per atom are small above 512 k-points such that using 512 or more k-points should provide stability for energy calculations for a structure of 1 atom. The structure of 64 atoms also displays stable energy calculations, albeit for a smaller number of k-point. This system shows stable energy calculations for 27 k-points. As seen here, it is a general rule that the larger the structure volume is, the less k-points are needed. This has do do with the Brillouin zone being smaller for larger systems, as discussed in Subsection 2.1.3. This is also the reason for no data for one k-point for the system of 1 atom, as the calculations did not converge.

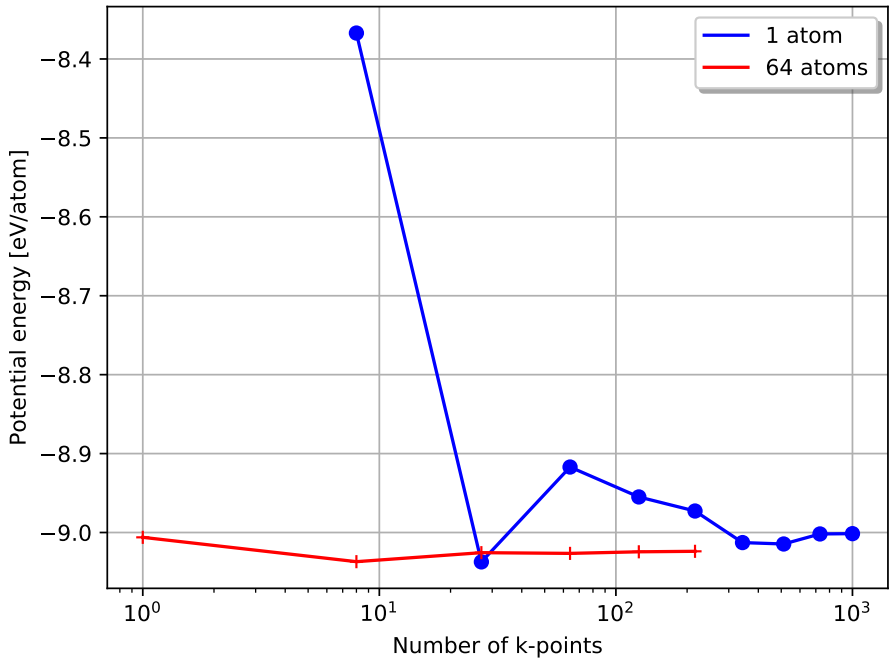

Figure 4.1: Potential energy per atom as a function of number of k-points for bulk bcc iron systems of 1 and 64 atoms.

Figure 4.2 shows how the energy calculations vary with different plane wave energy cutoffs and how they converge. At $E_{\text{cut}} = 600$ eV the energy per atom seems to converge for both systems, and calculations with energy cutoff above this value should be stable, given that the other parameters used also provide stability. It is also interesting to note that the energies per atom overlap for the two systems, as the values E_{cut} are the same. The number of available bands and the number of k-points for the two calculations are different, but these variables do not seem to impact the numerical value of the energy to a large extent.

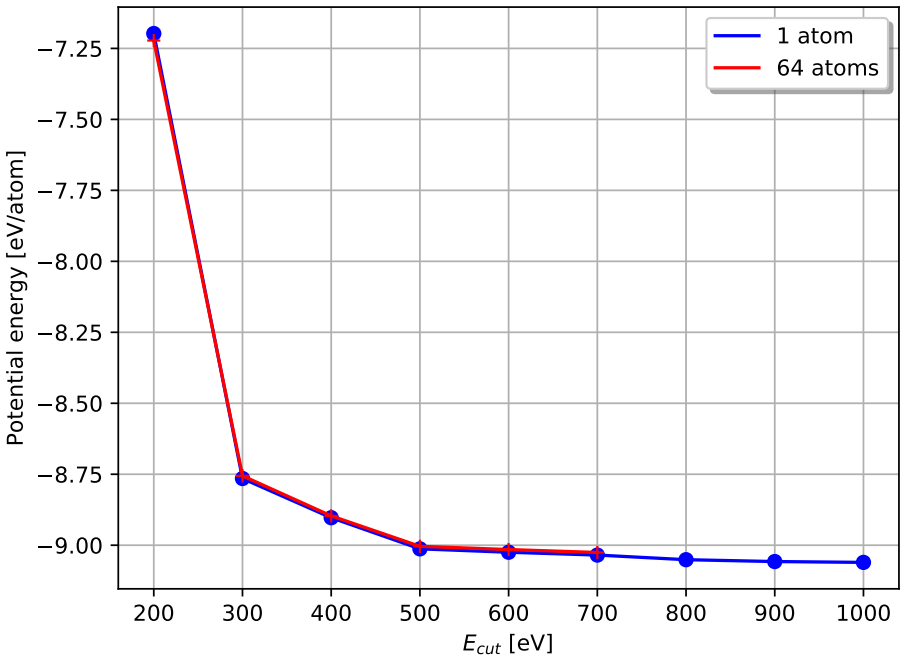

Figure 4.2: Potential energy per atom as a function of the plane wave energy cutoff, for bulk bcc iron systems of 1 and 64 atoms.

The last stability check done is for the value of $k_{\mathrm{B}}T$ in the Fermi-Dirac distribution (2.11). This smearing factor is checked in the temperature range from approximately 70 K to 6000 K, and Figure 4.3 shows that the calculations are stable within most of the temperature range. However, it is not necessary to use high temperatures for the following calculations, as an extrapolation to 0 K is done, and it should suffice to do calculations within the range of 200 K to 1000 K.

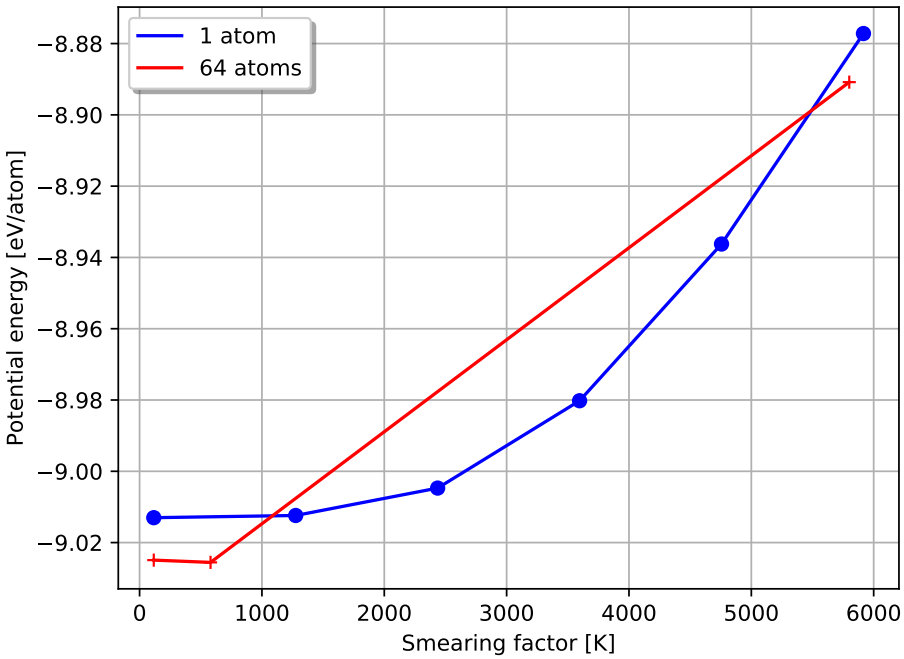

Figure 4.3: Potential energy per atom as a function of the temperature in the smearing factor for bulk bcc iron systems of 1 and 64 atoms.

4.2 Spin orientation and magnetic moment

Iron is a ferromagnetic material, meaning the the atom spins are aligned even with no external magnetic field, as discussed in Subsection 2.3.1. Therefore, it is interesting to investigate if the DFT energy calculations manage to predict whether iron is ferromagnetic or not. Three energy calculations are done for a bcc iron system of two atoms with periodic boundary conditions. One where the spins of the atoms are set to zero, one with the spins parallel and one with antiparallel spins. The numerical values of the magnetic moments are fixed through calculations, such that $|\boldsymbol{\mu}| = 2.2\ \mu_B$/atom for the parallel and antiparallel calculations and $|\boldsymbol{\mu}| = 0\ \mu_B$/atom for the non-magnetic calculations. All other parameters are kept consistent across the calculations, and the GPAW input parameters are set to be $E_{\text{cut}} = 600$ eV, nbands $= -5$, $k_{\text{B}}T = 0.05$ eV and 512 k-points. The calculated energies are presented in Table 4.2.

Table 4.2: Energies for different spin configurations for a 2 atom iron system.

	Energy [eV/atom]
Zero spins	−8.48
Parallel spins	−9.05
Antiparallel spins	−8.59

No spin configuration provide unreasonable energies, but the lowest energy is as expected associated with the parallel spin configuration. It is interesting to note that it seems as if this system is more stable with antiparallel spins than with zero spins.

The numerical value of $\boldsymbol{\mu}$ is also investigated. Energy calculations for the two atom system with parallel magnetic moments are carried out for different values of the magnetic moment, with the same GPAW input parameters as used previously. These results are shown in Figure 4.4. An energy minimum is observed between 2.0 and 2.5 Bohr magnetons per atom, which agrees well with the results obtained by J. Kübler [50], where the local spin density functional approximation was used. Other calculations have found $|\boldsymbol{\mu}| = 2.15\ \mu_B$/atom [51, p. 84] which also agrees with these results.

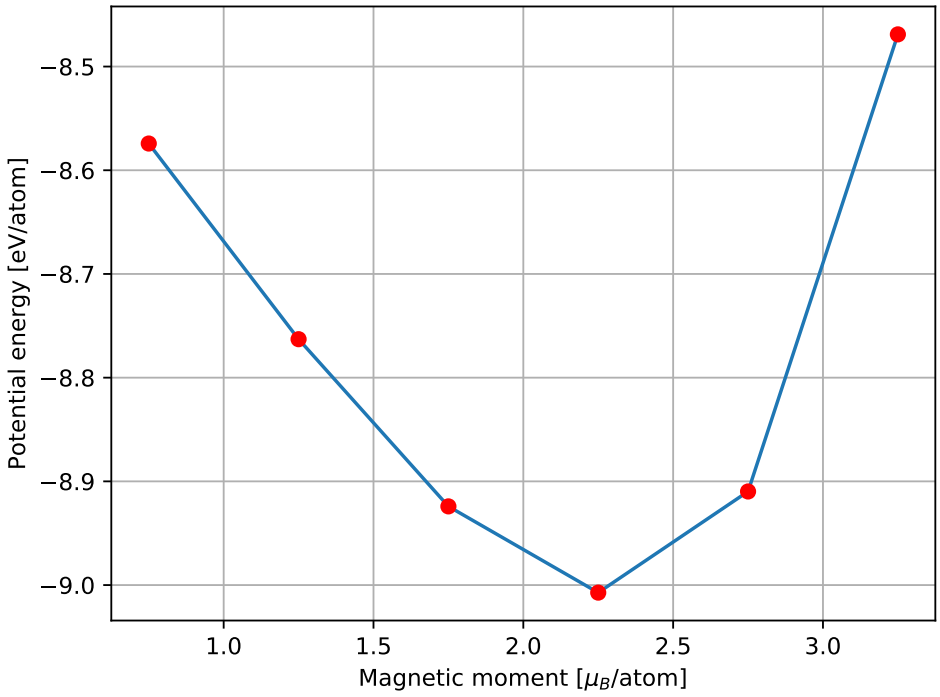

Figure 4.4: Potential energy per atom for a two atom structure of bulk bcc iron with parallel magnetic moments.

As the magnetic moment of pure iron has been investigated, the next step is to analyze the magnetic moment of bcc iron-silicon alloys. A total of 108 structures are relaxed, and the magnetic moments are calculated. The way these DFT calculations are done is further explained in Subsection 4.4.1. The results are shown in Figure 4.5. The red circles indicate the calculated magnetic moments per atom, while the blue line represents the contribution from the iron atoms to the magnetic moment if the configuration and the silicon-iron atomic spin interactions are ignored. It is seen that the magnetic moment per atom for X(Si) = 0 is in agreement with the magnetic moment previously found for the pure iron system. Also, at X(Si) = 1 the magnetic

moment is zero, which is as expected for a non-magnetic material in zero external magnetic field. Structures with close to zero magnetic moment are seen for X(Si) = 0.5, and several structures with higher silicon concentrations display similar behavior. It seems as if the silicon concentration is high enough, the diamagnetic properties of silicon give rise to non-magnetic structures. This property depends on the atomic configuration of the structure, as some of the structures with higher silicon concentrations have non-zero magnetic moments. The diamagnetic properties of the silicon atoms are observed for the rest of the structures, as the magnetic moments per atom is smaller than the expected magnetic moment of the isolated iron atoms for all except one structure. The structure having a higher magnetic moment is seen above the blue line for X(Si) = 1/9, and is identified as being one silicon atom and 8 iron atoms.

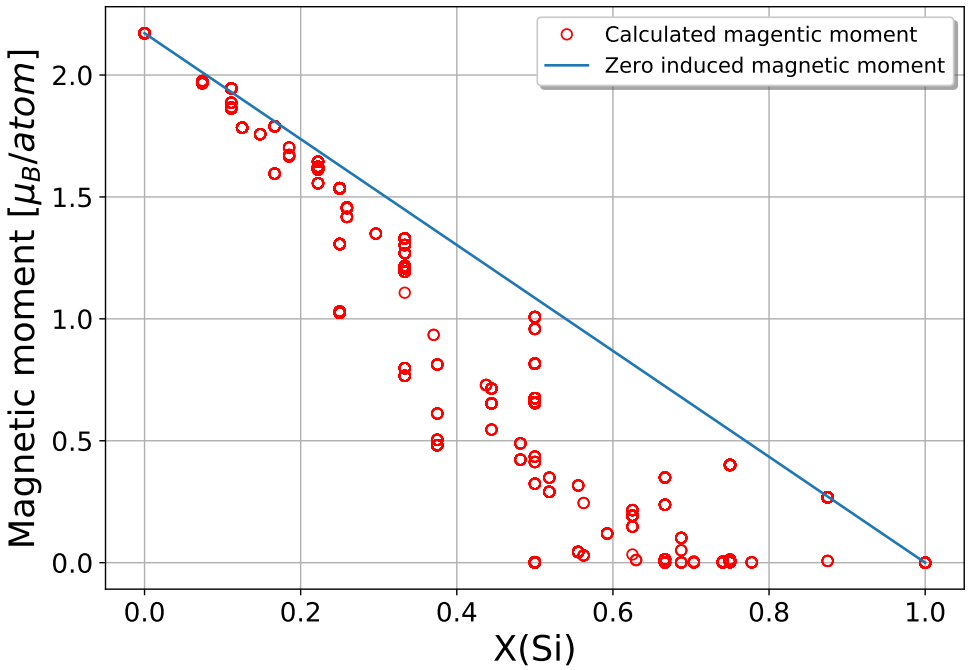

Figure 4.5: Magnetic moment per atom for bcc iron-silicon alloys with different structure sizes and varying silicon concentrations.

4.3 Electronic band structure and density of states

This section presents the calculated electronic band structures and DOS for iron and silicon. A single atom with periodic boundary conditions in a bcc structure is used to represent the bulk iron system. The GPAW parameters used for these calculations are the same as for the structure of two iron atoms studied in Section 4.2. The electronic band structure for iron is shown in Figure 4.6a, where the dashed line at zero indicates the Fermi level. All energies are shifted with respect to the Fermi level. The Fermi level for the system studied lies inside several bands, indicating that the material is a metal. The calculations are spin-polarized, creating two different sets of

bands for spin up and spin down. The result for the band structure of iron agrees well with other works [52].

The DOS for the iron bulk is also calculated, using the same parameters as for the calculation of the electronic band structure. The results are shown in Figure 4.6b, where the red line indicates the Fermi level. The Fermi level lies inside a region with non-zero DOS, which again supports the argument that iron is a metal. This is as expected from the analysis of the band structure.

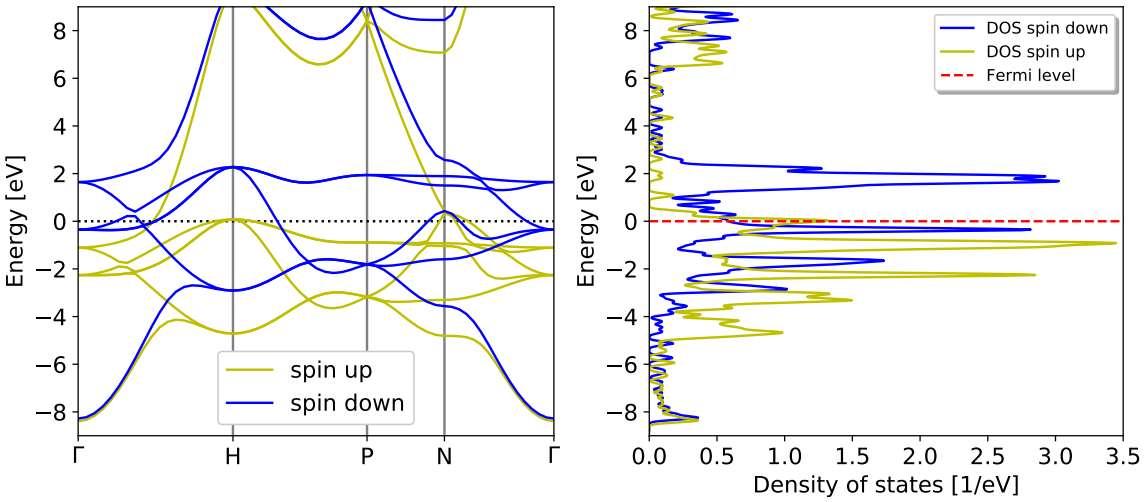

(a) Electronic band structure. **(b)** DOS.

Figure 4.6: Electronic band structure and DOS for bulk bcc iron. Energies are shifted with respect to the Fermi level.

Figure 4.7a shows the electronic band structure for bulk diamond cubic silicon. The calculations are done in the same way as for iron, except that the energy cut-off is set to 400 eV and the calculations are non-spin polarized. In contrast to iron, silicon has band gaps and is known to be a material with an indirect adsorption process [8, p. 190]. This is often referred to as an indirect band gap, where the minimum energy gap between the valence band and the conduction band involves electrons and holes separated by a wave vector which is seen between the Γ-point and to the left of the X-point. This is also observed in previous works where calculations for the silicon band structure were done [53].

Analyzing the electronic DOS for silicon in Figure 4.7b it is seen that silicon has many states around the Fermi level. These peaks in the DOS correspond to regions with a high density of electrons and holes in the band structure, where the band structure is flat over a significant range in the wave vectors. The Fermi level, indicated by the red dashed line, lies in a region of zero DOS, indicating that silicon is a semiconductor or an insulator. Silicon has been thoroughly studied, and it is well known that it is a semiconductor due to the band gap being small compared to the band gap in insulators [8, p. 186].

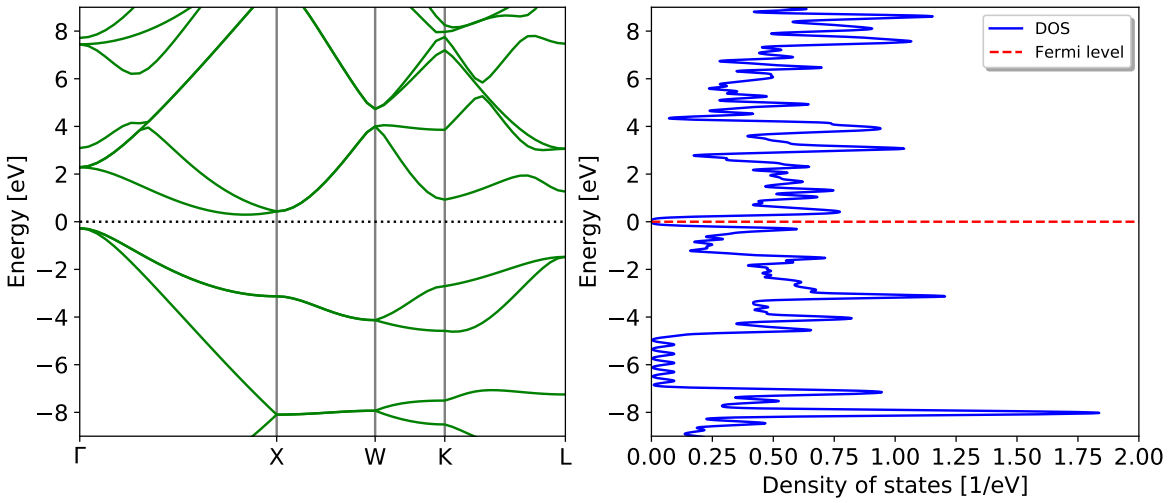

(a) Electronic band structure. **(b)** DOS.

Figure 4.7: Electronic band structure and DOS for bulk diamond cubic silicon. Energies are shifted with respect to the Fermi level.

4.4 Cluster expansion

As the GPAW input parameters and certain material properties of iron and silicon have been investigated, more DFT calculations are done for an alloy of iron and silicon, to provide input to a CE and obtain the ECIs. The statistical outcomes of the CE, the obtained ECIs, and the formation energies as predicted by DFT and the CE are discussed.

4.4.1 Evaluation of the CE

The input structures of the CE model are made up of initial and relaxed structures of iron and silicon. A total of 83 initial structures are used, with X(Si) ranging from 0 to 0.525. The atoms are arranged in a bcc lattice with periodic boundary conditions, and the number of atoms in the structures varies from 2 to 27. An overview of the different sized structures used are given in Table A1, Appendix A. The final structures are obtained through DFT calculations, where the BFGS algorithm is used to relax the structures. The relaxation process is considered done when no atom in the structure is subjected to forces greater than 25 meV/Å. As shown in Section 4.1, the energy calculated by DFT for a given structure varies with the GPAW input parameters. It is therefore essential to keep the parameters used consistent across all calculations. The parameters used for these DFT calculations are $E_{\text{cut}} = 600$ eV, nbands $= -100$, $k_{\text{B}}T = 0.1$ eV and $k_{\text{dens}} = 5.4$ Å^{-1}. The xc functional used throughout the calculations is the PBE functional. The initial magnetic moment of the silicon atoms is set to 0 μ_B/atom, while for the iron atoms it is set to 2.2 μ_B/atom. The magnetic moments are calculated in all iterations of each BFGS step.

An evaluation of the CE for the iron-silicon alloy is shown in Figure 4.8. In this figure, a red circle indicate the CE predicted energy for a structure using the ECIs from the CE obtained by a

fit to the energies of all structures excluding the one corresponding to the circle. Likewise, a blue circle shows the predicted energy of a structure where the energy of this structure is included in the fit to calculate the ECIs. The CV score from this CE is 23.8 meV/atom. This CV score is higher than what was obtained in other works where other alloys were investigated [47][54]. It should be noted that the numerical value of the CV score depends on the energy of the pure elements. Iron is an element associated with high absolute value DFT energy, such that alloys containing iron could give a higher CV score, as seen from the definition of the CV score, Equation (2.67). Circles on the red line show that the DFT and CE predicted energies match to a large extent, as the predictive power of the CE is not the same for all structures. Also worth noting is that the structures with the lowest energies have the largest iron concentration, and the data point with the lowest energy is pure bcc iron.

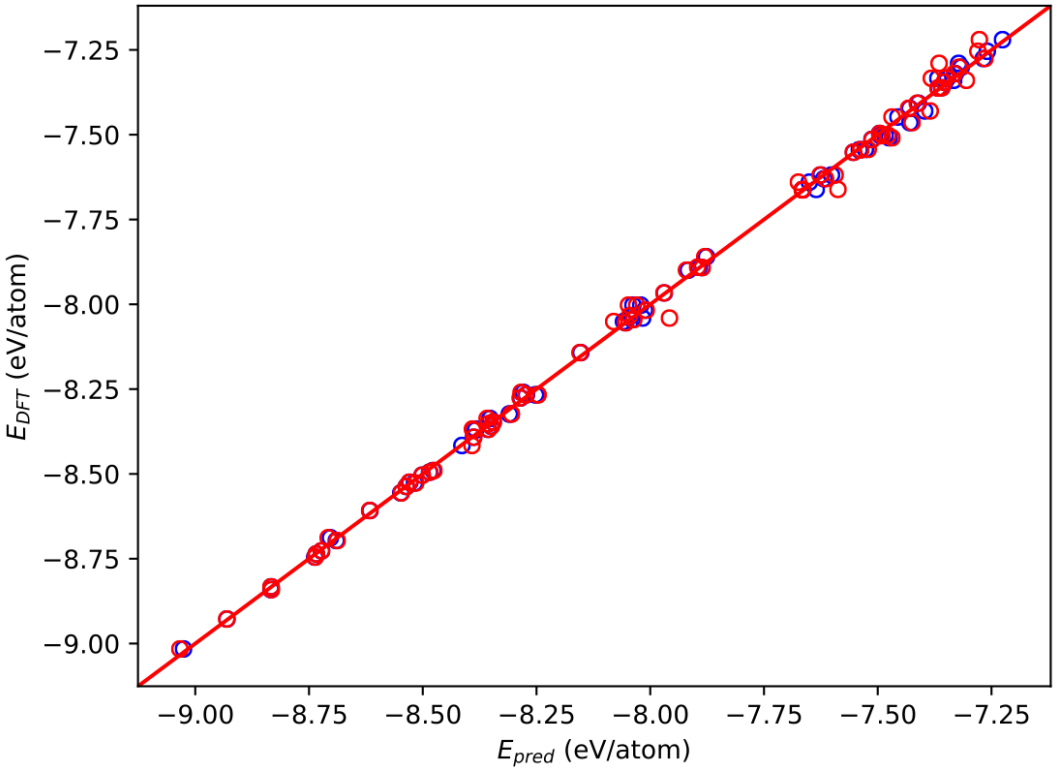

Figure 4.8: DFT energies and CE predicted energies. The blue circles are the energies as predicted by a fit to the energies of all the structures. The red circles are the energies as predicted by a fit to the energies of all other structures. The red line indicates where the CE energies are equal to the DFT energies.

Figure 4.9 shows the residuals and the leave-one-out residuals for the CE. As expected, most of the residuals are smaller in absolute value than the leave-one-out residuals. This is due to the CE being most accurate when predicting the energies for structures similar to those included in the input set of structures. This is also reflected in Figure 4.8, where some of the red circles are further away from the red line compared to the blue circles. The largest residuals are found for structures with higher silicon concentrations. This could be due to the fact that all structures in

the CE are bcc, while pure silicon favors a diamond cubic arrangement of atoms. On the right-hand side of Figure 4.9, the distribution of the residuals is plotted. Even though this distribution does not resemble a typical normal distribution, it highlights that no systematic over or under prediction is done in terms of the predicted energies from the CE. The RMSE obtained from the residuals is found to be 13.4 meV/atom. Based on this it can be concluded that the average predictive power of the CE model is acceptable.

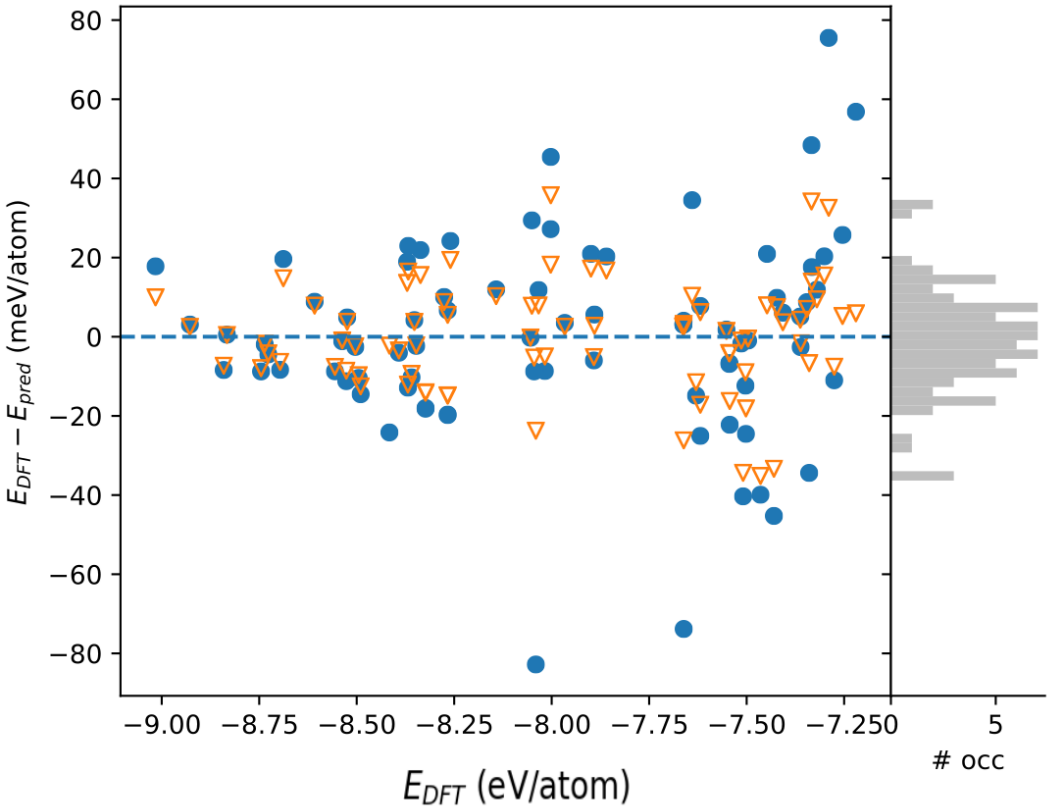

Figure 4.9: Residuals for the CE predicted energies. The circles are leave-one-out residuals, and the triangles are residuals.

4.4.2 Effective cluster interactions

Having obtained ECIs through the CE method, which gives accurate energy predictions, the ECIs are further investigated. To identify the characteristics of the ECIs, an ECI naming scheme is used. A cluster with name cA_Bnn_C is a cluster of A atoms, where B is the largest internal distance in the cluster with regards to nearest neighbors and C is an identification number.

The configurational variable, σ, is -1 for silicon and 1 for iron. Using this in conjunction with the sign of the ECI energy, the composition of the ECI can be identified, and the configurations which are most energetically favorable can be found. If the ECI energy is positive, a negative characteristic function is needed to reduce the configurational energy (2.66), and if the ECI energy is negative, a positive characteristic function reduces the energy. In the evaluation of the ECIs,

the zero- and one-body clusters, shown in Figure 4.10, are trivial in the sense that they only contain zero or one atom. Nevertheless, these ECIs contribute to the total energy, as they are the largest in terms of eV/atom. The four-body ECIs shown in Figure 4.12 are harder to interpret, so the two- and three-body ECI will be discussed. It should be noted that the contribution to the configurational energy from the four-body ECIs is comparable to that of the two- and three-body ECIs.

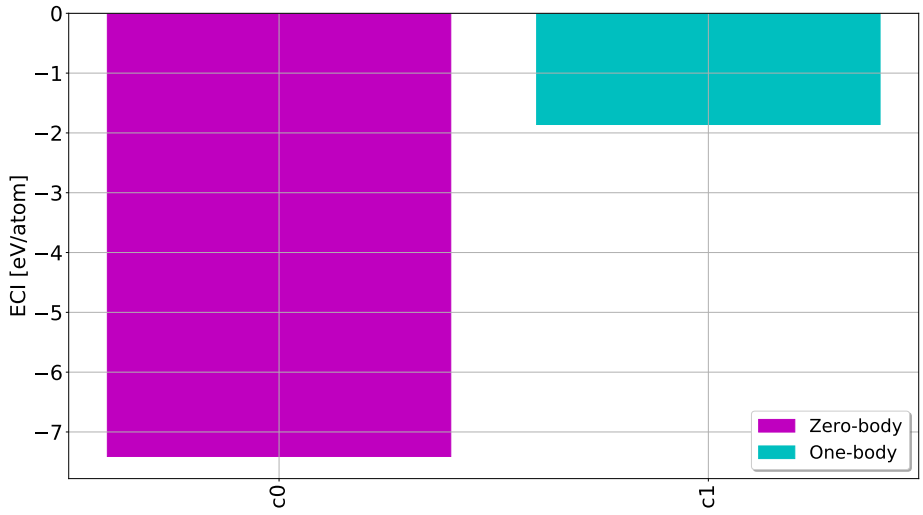

Figure 4.10: The zero- and one-body ECIs from the cluster expansion.

Amongst the two-body clusters shown in Figure 4.11, the two clusters which contribute the most to the energy are c2_01nn_0 and c2_04nn_0. c2_01nn_0 consists of two atoms within nearest neighbor distance, and the sign of the ECI is positive. From the discussion above, this cluster must contain one iron and one silicon atom, as to get a negative contribution to the configurational energy. On the other hand, the ECI c2_04nn_0 has a negative sign, with the two atoms within fourth nearest neighbor distance from each other. This means that the cluster formed must consist of two iron atoms or two silicon atoms.

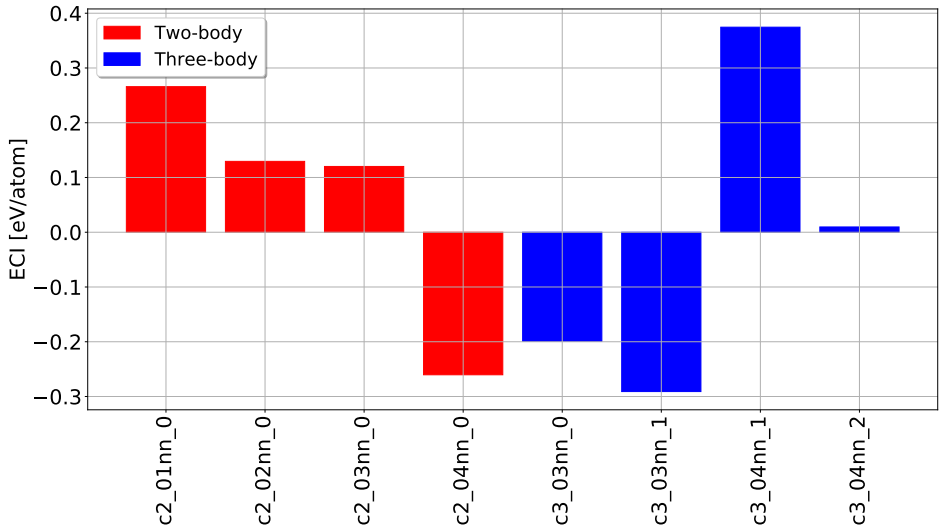

Figure 4.11: The two- and three-body ECIs from the cluster expansion.

For the three-body clusters, the two largest ECIs are the c3_03nn_1 and c3_04nn_2. The first of these clusters has negative energy and is made up of three atoms within third nearest neighbor distance. To get a negative contribution to the configurational energy it must consist of three iron atoms or one iron atom and two silicon atoms. The c3_04nn_2 is configured in the same way, except that the atoms are located within fourth nearest neighbor distance from each other. The sign of this ECI is positive, such that the cluster must contain two iron atoms and one silicon atom or three silicon atoms.

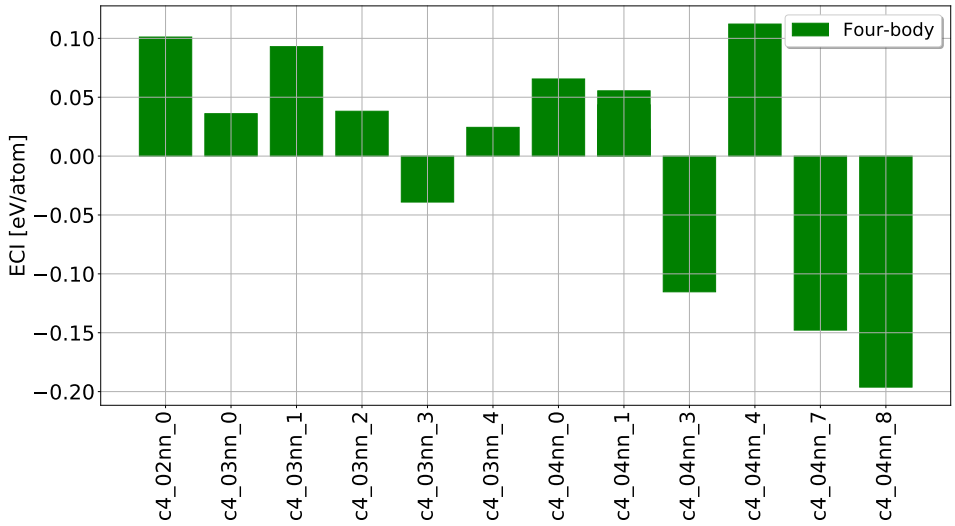

Figure 4.12: The four-body ECIs from the cluster expansion.

As discussed in Subsection 2.6.3 the selection algorithm used for obtaining the ECIs set many of the ECIs to zero as only a finite number of ECIs can be used when calculating the configurational energy. In this CE model a total of 22 ECIs are non-zero. The number of non-zero ECIs included is largely dependent on the alloy system studied, as well as the selection algorithm. This is seen in previous works where a total of 9 non-zero ECI were used in a CE model developed for fcc aluminium-magnesium alloys [7].

4.4.3 Formation energy

The final evaluation of the CE model is to compare the formation energies for the 83 iron-silicon structures from the DFT energies and the CE predicted energies. The formation energies per atom are calculated using Equation (2.15), where the energies for the pure silicon and iron bulks are set to be those calculated by DFT. The results are shown in Figure 4.13, where the convex hull is fitted to the DFT formation energies. The formation energies in the shaded region are only from DFT, and the structures within this region were not included in the CE for calculating the ECIs which the CE predicted formation energies are based on. All except one of the formation energies, excluding the formation energy for the pure silicon and iron structures, are negative. This shows that it is energetically favorable for iron and silicon to form certain mixed structures instead of segregating in the alloy.

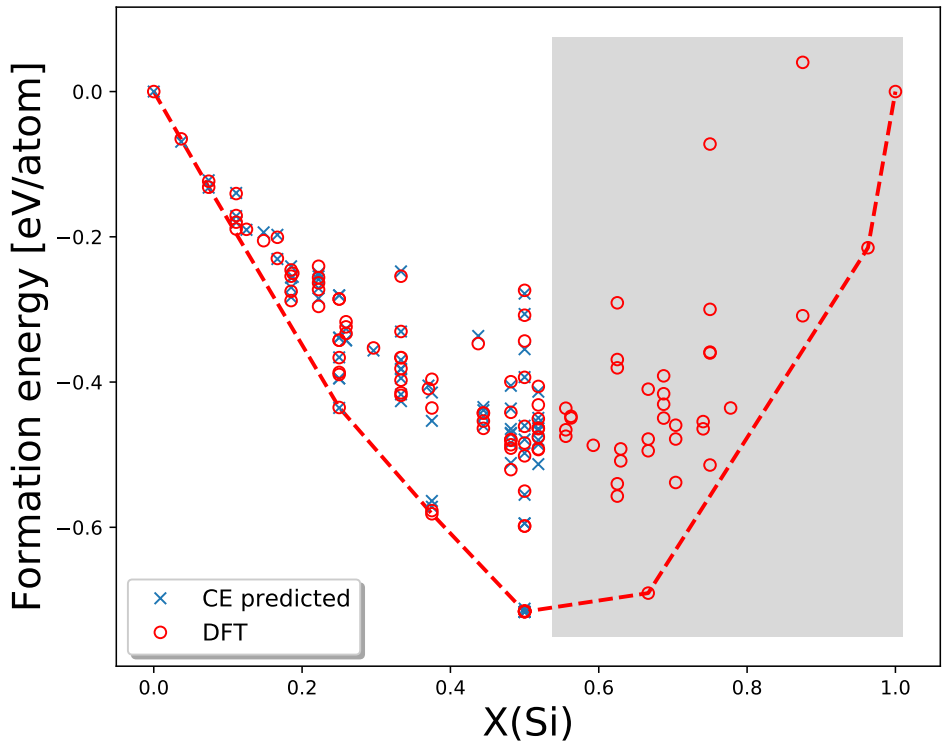

Figure 4.13: Formation energy and convex hull for the iron-silicon systems, using predicted energies from the CE and DFT energies.

In the interior of the convex hull, the CE predicted formation energies differ from the DFT formation energies to a varying extent, depending on the structure. What is most important is that the CE predicted formation energies are precise for the ground states of the iron-silicon alloy. Two of the ground states can be seen on the convex hull at X(Si) = 0.5, Fe_4Si_4 (FeSi), and X(Si) = 0.25, $Fe_{12}Si_4$ (Fe_3Si). The structures are displayed in Figure 4.14a and 4.14b respectively. Worth noting is that the structure found to be om the convex hull for X(Si) = 0.5 has alternating planes of silicon and iron atoms in the (100) directions. For these two structures, the formation energies calculated from DFT energies and from CE predicted energies are an excellent match, as the crosses lie inside the circles.

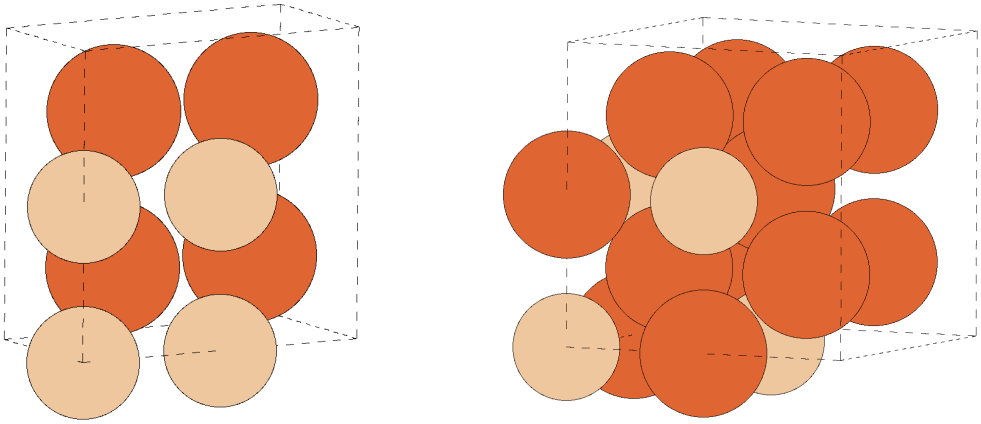

(a) Fe_4Si_4. **(b)** $Fe_{12}Si_4$.

Figure 4.14: The two structures with lowest formation energy for X(Si) = 0.5 and X(Si) = 0.25. Iron atoms are orange and silicon atoms are beige.

4.5 Monte Carlo simulations

Having evaluated the CE, the ECIs obtained are used to do MC simulations in the canonical and semi-grand canonical ensembles. This way, thermodynamic properties for larger iron-silicon systems can be examined. The predicted ground states for silicon concentrations of 25 % and 50 % are obtained by MC simulated annealing in the canonical ensemble. These ground states are then used in MC simulated heating, and calculations are done to model the dissolution of Fe_3Si and FeSi structures in pure iron phase surroundings. Following this, phase boundary tracing is done to obtain a part of the phase diagram for the iron-silicon alloy.

4.5.1 Simulated annealing

In this subsection, MC simulations are used to obtain the predicted ground states of the iron-silicon alloy at two different concentrations. This is done by cooling down bcc iron-silicon structures of 1024 atoms with constant concentrations from 5000 K to 100 K. The initial structure at 5000 K is a random configuration of iron and silicon atoms, at the given concentration. The calculations are done in the canonical ensemble, and the total number of particles is kept fixed. The two concentrations examined are X(Si) = 0.25 and X(Si) = 0.5.

Figure 4.15a displays the final structure from simulations with X(Si) = 0.25. Here, each silicon atom has iron atoms as its nearest neighbors, which is consistent with the two-body cluster c2_01nn_0. Two-body clusters consisting of iron and silicon at second nearest neighbour distance are also observed, corresponding to the c2_02nn_0 cluster. These clusters are also accompanied by clusters with larger nearest neighbour distances, but these are harder to interpret. The structure corresponds to a repeated version of the structure found on the convex hull for X(Si) = 0.25, shown in Figure 4.14b, supporting the argument that this is a ground state for this concentration. The repeating pattern of this structure is a bcc cube with iron on the corners, and alternating

silicon and iron atoms in the center. This corresponds to the $D0_3$ structure observed for Fe_3Si at low temperatures [55], which was obtained through experimental annealing. Obtaining the Fe_3Si structure is also as expected from the phase diagram for iron-silicon alloys for X(Si) = 0.25 [56, p. 713]. It is shown that the $D0_3$ structure forms at this concentration for temperatures sufficiently below the melting point.

Figure 4.15b shows the final structure of the MC simulations with X(Si) = 0.5. Here each silicon atom has four iron atoms and four silicon atoms as its nearest neighbors. This corresponds to the two-body cluster c2_01nn_0 for the silicon and iron nearest neighbors, but not for the iron-iron and silicon-silicon nearest neighbors.

This phase has alternating silicon and iron planes in the (110) directions. Due to this, the structure might not at first be suspected to be a ground state of the system when examining its atomic configuration with respect to the ECIs. If the planes instead were in the (100) direction, each silicon atom would only have iron atoms as its eight nearest neighbors, being more consistent with the c2_01nn_0 cluster. The reason for the planes being oriented in the (110) directions could be due to the packing of the bcc lattice. Planes in the (110) direction give the highest atomic density as they are the most closely packed planes.

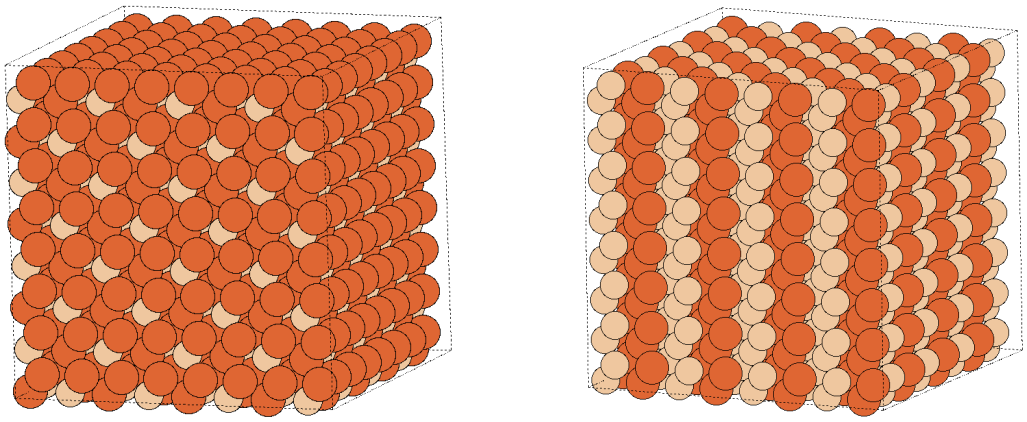

(a) X(Si) = 0.25 **(b)** X(Si) = 0.50

Figure 4.15: The two final structures from MC simulations when cooling down iron-silicon systems containing 1024 atoms. The orange atoms are iron, while the beige atoms are silicon.

The structure obtained from simulated annealing with X(Si) = 0.5 was not included in the set of structures used for developing the CE model. The smallest structure replicating the (110) alternating layers of iron and silicon consists of 16 atoms. To investigate if this structure could be a ground state for X(Si) = 0.5, DFT calculations are done. The GPAW input parameters used are the same as the ones used in the DFT calculations done for developing the CE. The formation energy for the structure with alternating (110) planes of iron and silicon is found to be -0.717 eV/atom, while the formation energy for the structure observed on the convex hull for X(Si) = 0.5, with alternating iron and silicon planes in the (100) directions, is -0.716 eV/atom.

From these results it is seen that the formation energies for the structures with (110) and (100) planes are similar in value and that the configuration with (110) planes has the lowest formation energy. Interestingly, it seems as if the energy of the iron-silicon system at this concentration is largely non-dependent on the spatial orientation of the iron-silicon layers.

4.5.2 Simulated heating

Having obtained the ground states predicted by simulated annealing for X(Si) = 0.25 and X(Si) = 0.5, the next step is to study the dissolution of the Fe_3Si and the FeSi structures in iron encasements through MC simulated heating. Structures as discussed in Subsection 3.3.2 and illustrated in Figure 3.2a and Figure 3.2b are used with MC simulations in the canonical ensemble. This is done to analyze how the atoms displace to reduce the total energy and to extract thermodynamic properties. The total number of atoms is kept constant at 128000, resulting in a 40x40x40 bcc structure, where the basis consists of two atoms. The size of the cubes and octahedra in the interior of the larger iron cube is changed across multiple simulations, changing the silicon concentration of the systems. Worth noting is that due to the restrictions on the geometry of the interior structures, it is not always possible to construct a cube and an octahedron containing the same number of atoms. The number of MC steps at each temperature is set to increase with the size of the interior structures. As more silicon atoms are introduced, the number of possible configurations for the system increases until X(Si) = 0.5, and the number of MC steps at each temperature is therefore set to be some constant times the number of silicon atoms in the structure.

When heating the structures the silicon and iron atoms start to switch positions to reduce the systems total energy throughout the MC simulations. The SOP is used as a measure of the dissolution process in the system and is obtained directly from the simulations. To normalize the SOP, the obtained SOP is divided by two times the number of silicon atoms in the structure.

The entropy is obtained by first calculating the free energy (2.24), where the integral is computed numerically using Simpson's rule [57, p. 257]. The total energy is obtained in the MC simulations using the ECIs from the CE, and the thermodynamic definition of the Helmholtz free energy (2.18) is used to calculate the entropy. The entropy is normalized as to better illustrate the change in entropy across different internal structure sizes and temperatures.

Firstly, the Fe_3Si systems are analyzed. The number of MC steps used at each temperature is 2000 times the number of silicon atoms. The temperature is increased from 50 K to 1000 K with varying increments in temperature. Figure 4.16 shows the normalized SOP and entropy for iron cubes containing Fe_3Si cubes of different sizes. At 50 K a significant number of silicon atoms have changed positions for all internal structure sizes, as seen from the SOP. This reveals that a cubic arrangement of Fe_3Si is not energetically favorable, even for low temperatures. The SOP starts to slowly increase in a linear fashion until 150 K. Above this temperature the SOP increases rapidly until it is close to unity. This effect is also reflected in the entropy, as a rapid

increase in the entropy is seen at the same time as the SOP tends towards unity.

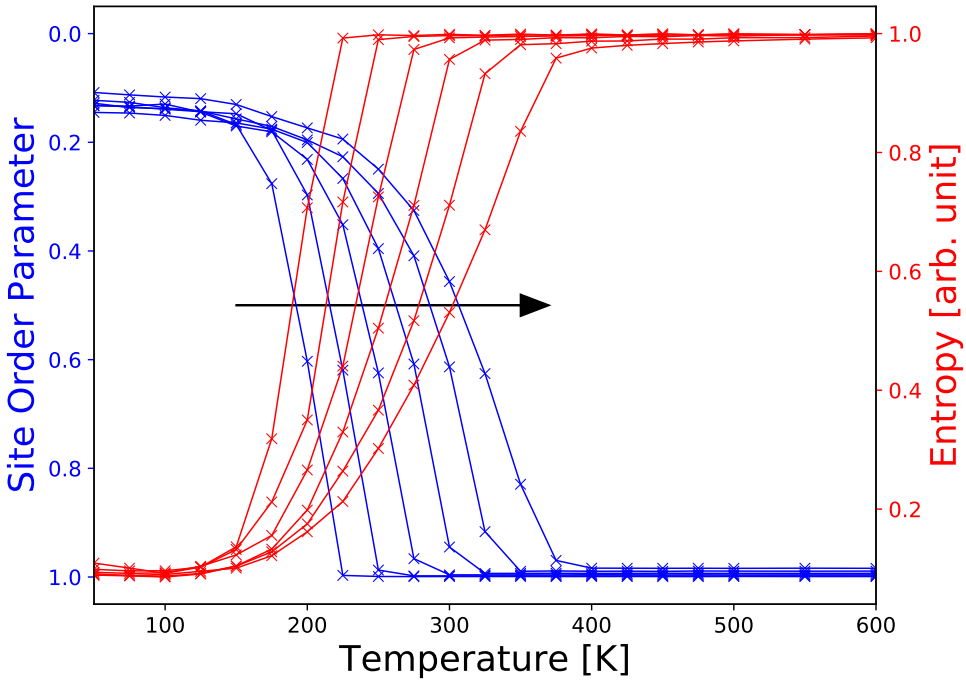

Figure 4.16: Normalized SOP and entropy for cubes of varying sizes of Fe_3Si inside an iron box. The crosses indicate the temperatures at which MC simulations are done. The arrow indicates the direction of increasing structure size.

Figure 4.17 shows the normalized SOP and entropy for Fe_3Si octahedra situated inside the iron cube. Below 150 K there is a significant difference between the displacement of atoms for Fe_3Si cubes and the octahedra. When Fe_3Si is constructed as an octahedron, zero or close to zero silicon atoms are displaced for temperatures below 150 K for all internal structure sizes. This shows that Fe_3Si arranged as an octahedron is more stable at low temperatures than Fe_3Si shaped as a cube. This could be due to the cubes having the (100) planes of the bcc structure exposed, as opposed to the octahedra which have the (111) planes exposed. There seems to be an excellent match between the SOP and the entropy across all sizes.

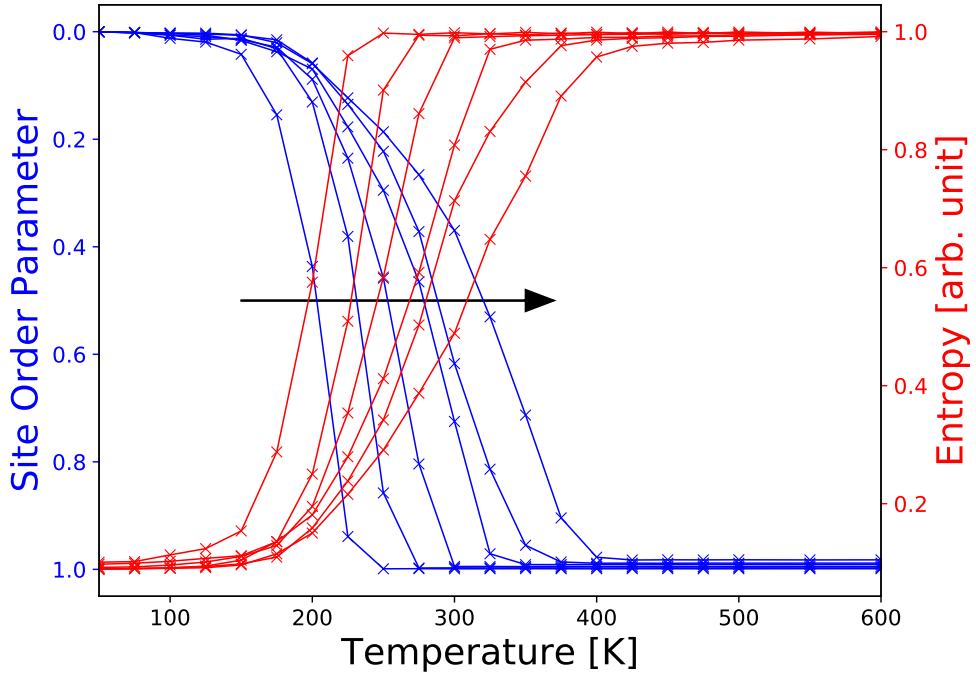

Figure 4.17: Normalized SOP for octahedra of varying sizes of Fe_3Si inside an iron box. The crosses indicates the temperatures at which MC simulation are done. The arrow indicates the direction of increasing structure size.

For the FeSi systems, MC simulations are done in much the same way as for the Fe_3Si systems, but the internal cubes and octahedra are bcc FeSi. The temperature range is changed, as the simulations are done from 50 K to 1500 K. Also, the number of MC steps done at each temperature is increased to 10000 times the number of silicon atoms for the cubic structures, and 3000 times the number of silicon atoms for the octahedra.

Figure 4.18 shows the normalized SOP and entropy for different sized internal FeSi cubes at different temperatures. For low temperatures all structures immediately have displaced a noticeable amount of silicon atoms, showing that only a small amount of thermal energy is needed for the FeSi cube to deform. This is the same case as for the Fe_3Si cubes. For the smallest structure the entropy is seen to decrease in the range 175 K to 200 K. From the definition of the entropy (2.18) this could correspond to a decrease in internal energy for increasing temperatures, as the free energy can not decrease when thermal energy is added to the system. At this drop in entropy, a rise in the SOP for this structure is seen. This could mean that the decrease in entropy corresponds to the internal cube changing shape to a more energetically favorable configuration, such that the internal energy of the structure decreases. Also, it seems as if a barrier exists for this cube to change shape. If no barrier were present, the cube would have deformed to its more energetically favorable shape at the initial temperature of 50 K, and no drop in entropy would be seen.

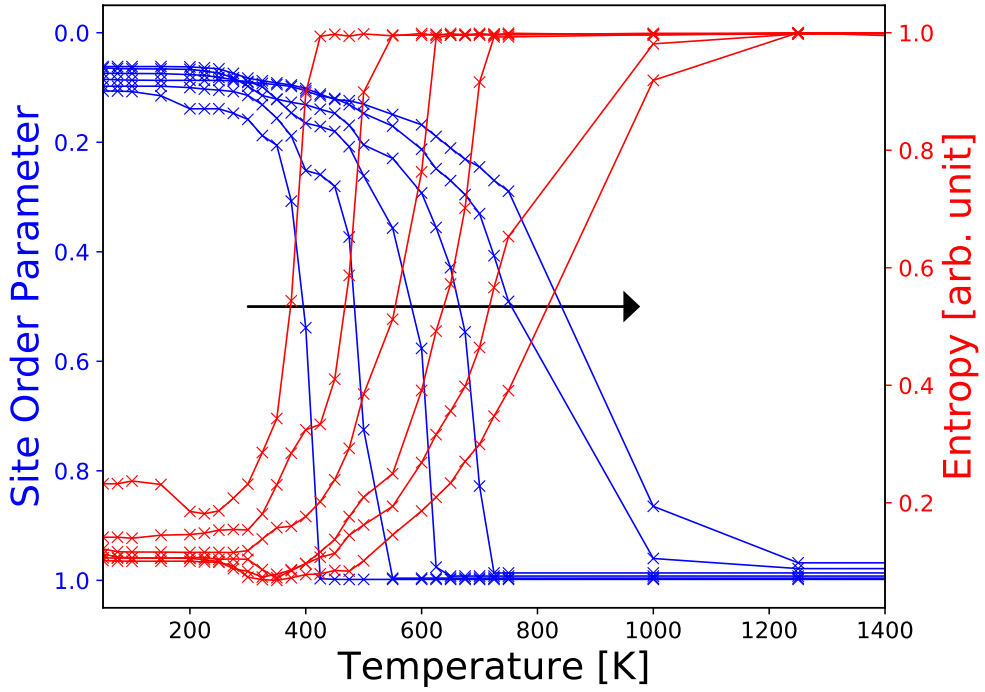

Figure 4.18: Normalized SOP and entropy for cubes of varying sizes of FeSi inside an iron box. The crosses indicate the temperatures at which MC simulations are done. The arrow indicates the direction of increasing structure size.

In Figure 4.19 the SOP and entropy for the iron enclosed FeSi octahedra are displayed. Much the same conclusions can be had for this system as for the FeSi cubes. What is interesting here is that this system displays a significantly different behavior compared to that of the Fe_3Si octahedra in Figure 4.17. It seems as if the FeSi structure is less stable, as a significant portion of the silicon atoms are displaced in these systems for temperatures below 200 K. From this it is possible to argue that the Fe_3Si octahedra are more stable than the FeSi octahedra for low temperatures.

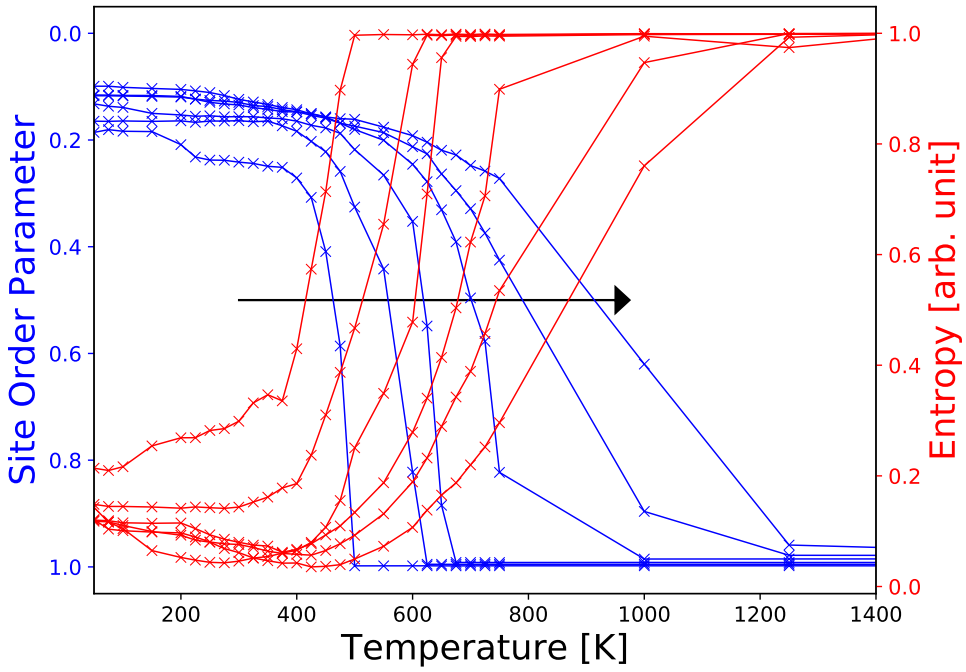

Figure 4.19: Normalized SOP and entropy for octahedra of varying sizes of FeSi inside an iron box. The crosses indicate the temperatures at which MC simulations are done. The arrow indicates the direction of increasing structure size.

From these results, it is observed that the Fe_3Si and FeSi cubes and octahedra have some common traits. The smaller structures seem to be the least rigid. When the temperature is increased these structures have most of their silicon atoms displaced before the silicon atoms in larger structures dissolute. The average distance from the silicon atoms to the iron surroundings increases with the size of the internal structure. Thus, the average silicon atom of a large internal structure requires more thermal energy to move outside of its initial structure than the average silicon atom needs in a smaller structure. A small difference occurs in the high-temperature limit of the SOP for different sizes of the internal structures. The smaller the structure, the closer the SOP tends towards unity. This could be due to the structures with more silicon atoms having a higher probability of having some silicon atoms at the initial temperature which are already in positions that reduce the total energy of the system. This results from the fact that the total number of atoms in the systems is constant across all internal structure sizes, such that the ratio between the number of atoms in the internal structure and the number of atoms in the surrounding iron cube increases for increasing internal system sizes. It is also evident that the temperature range in which the SOP tends towards unity is drastically different between the Fe_3Si and FeSi systems. This will be further investigated in the next subsection. It is shown that there are many similarities between the behavior of the SOP and entropy at higher temperatures. This is as expected when considering that thermal fluctuations increase the disorder in the systems analyzed, which is reflected both in the entropy and the number of silicon atoms that has moved

from their more orderly initial positions.

4.5.3 Critical temperature

Having studied the SOP and entropy for the Fe_3Si and FeSi cubes and octahedra, it is interesting to compare the temperature regions in which the SOP increases rapidly for these phases. A critical temperature, T_c, can be defined as the temperature for when the normalized SOP is 0.5. Therefore, T_c can represent the temperature at which a system changes from an ordered to a disordered state, where half the silicon atoms have dissolved. T_c for the structures is obtained through interpolation of the SOP.

Figure 4.20 shows these critical temperatures for the four different systems, for different sizes measured in the number of formula units in the initial interior structure. Following the previous discussion about the SOP, it is clear that lower temperatures are needed to displace half of the silicon atoms in the smaller structures, compared to the temperature needed to displace half the silicon atoms in the larger structures. This shows that the dissolution process of the cluster inside is temperature and size dependent for combinations of both phases constructed as octahedra and cubes.

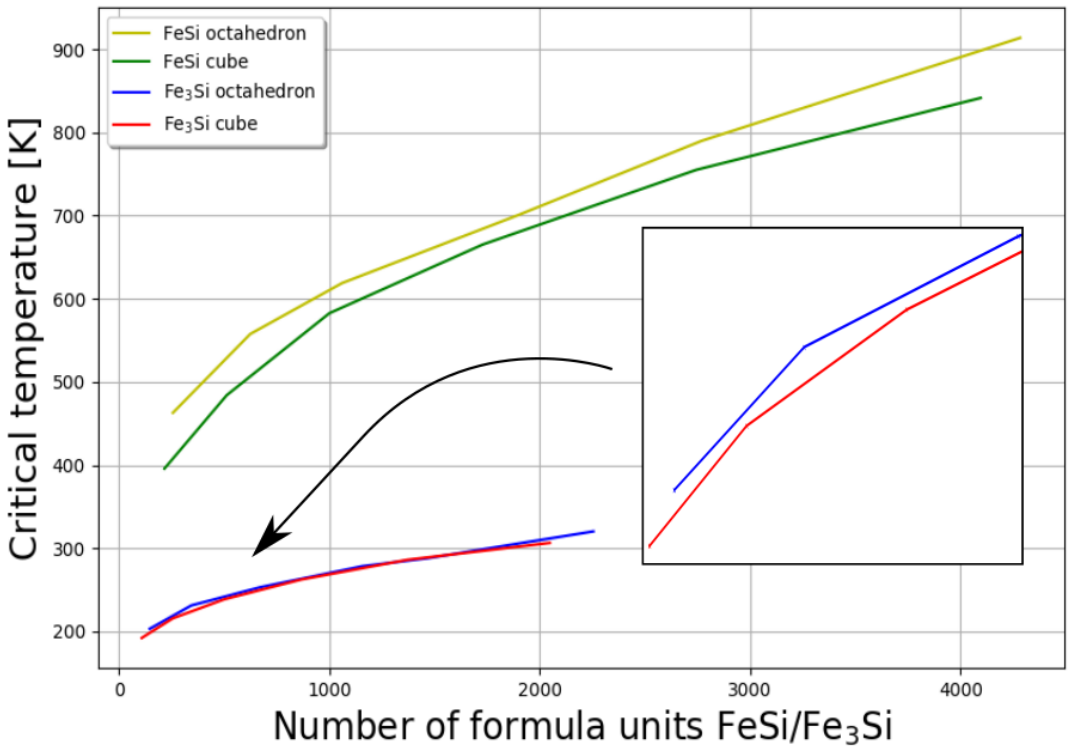

Figure 4.20: Critical temperatures for the Fe_3Si cubes and octahedra inside an iron box.

It is interesting to note the behavior of T_c for the smaller internal structures. Both for the FeSi and the Fe_3Si systems, T_c for structures containing a phase of approximately 2000 atoms or

less are less stable if constructed as a cube than if constructed as an octahedron, due to T_c being smallest for the cubes. Also, the FeSi cubes have a lower T_c compared to the critical temperatures for similarly sized octahedra across all structure sizes. The cubes have the (100) planes of the bcc structure exposed, while the octahedra have the (111) planes exposed. This difference in T_c could be due to less thermal energy being needed to dissolute silicon atoms on (100) planes than on (111) planes. It is important to note that if this is the only effect altering the T_c of the similarly sized octahedra and cubes, it should be consistent for all sizes. This is not the case, since for larger internal Fe_3Si structures, T_c is essentially the same for the octahedra and the cubes.

One major difference between the Fe_3Si and the FeSi phases is the range of T_c across all structure sizes. The FeSi phase requires substantially higher temperatures to displace half the silicon atoms, as seen by the large gap in T_c between the Fe_3Si systems and the FeSi systems. This shows that the FeSi phase is the most stable phase out of these two phases when the thermal energy in the systems is increased. The FeSi phase has more silicon atoms per volume than the Fe_3Si phase. It could therefore be easier for the silicon atoms in the Fe_3Si phase to dissolve into the surrounding iron cube, which is reflected in T_c being lower for the Fe_3Si phase.

It is interesting to compare the behavior of the SOP through the critical temperature and the temperature at which the heat capacity is at its peak value. The heat capacity is calculated numerically using Equation (2.25), by taking the derivative of the energy with respect to the temperature. T_m is defined as the temperature corresponding to the maximum of the heat capacity. Figure 4.21 shows a comparison between the two aforementioned temperatures. Worth noting is that from the discussion about the critical temperature, it is known that the smaller internal structures have the lowest critical temperatures. For the Fe_3Si systems T_m and T_c match well. T_c is based on the observed displacement of atoms, as it is calculated from the normalized SOP. T_m is also based on the disorder in the systems, as the heat capacity is proportional to the first derivative of the entropy with respect to temperature, as shown in Equation (2.26). From the previous discussion about the SOP and entropy, it is known that for these systems, the entropy and SOP match to a large extent. It is therefore not a surprise that T_m, even though it is calculated directly from the energy, reflects the behavior of the SOP. This is also the case for the systems containing smaller internal FeSi cubes and octahedra. For the larger FeSi systems T_c and T_m do not match. While T_c increases, T_m flattens out for increasing internal system sizes. The slope of the SOP for these larger sizes is less steep, as seen in Figure 4.18 and 4.19, such that the interpolation scheme used for calculating T_c could be less precise for these larger internal FeSi structures.

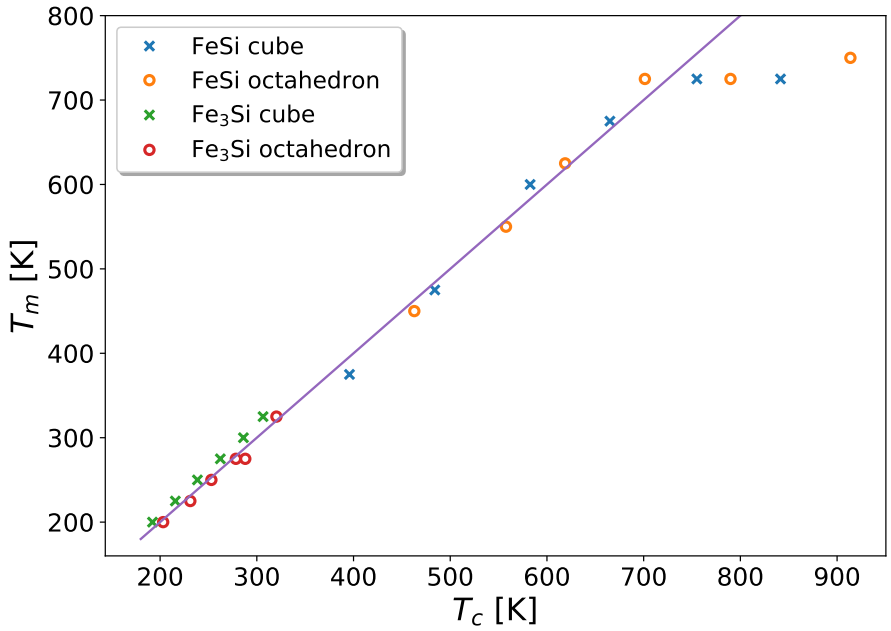

Figure 4.21: Critical temperatures and temperatures corresponding to maximum heat capacity for the FeSi and Fe_3Si cubes and octahedra inside an iron encasement. The blue line indicates where the critical temperature equals the temperature of maximum heat capacity.

4.5.4 Visualized dissolution of Fe_3Si and FeSi.

Having analyzed the behavior of the two phases through the SOP, entropy, and critical temperature, the atom trajectories from the MC simulations are investigated. Four structures, one from each of the four previously discussed cases, are chosen to illustrate the dissolution processes. First the Fe_3Si phase is analyzed. Figure 4.22 illustrates the dissolution of an Fe_3Si cube inside the surrounding iron cube. Already at 50 K, the cube is deformed, however no silicon atoms have dissolved into the iron encasement. This agrees well with the results for the SOP in Figure 4.16, where the SOP is shown to be non-zero for 50 K. Initially, the structure only has its (100) planes exposed. As thermal fluctuations are introduced the structure favors a spherical shape. The atoms on the corners of the cube are more exposed, and these atoms dissolve first. At 150 K some of the silicon atoms have started to move into the exterior iron cube, and the spherical shape in the center is maintained. At 225 K, the temperature is close to T_c for this size, and approximately half of the silicon atoms are displaced, and many of them have dissolved towards the boundary of the total structure. As expected from the previous results, all silicon atoms are displaced at 1000 K, and a random distribution of the silicon atoms is seen within the structure. This is as expected from the analysis of the SOP. Note that this is also the case at high temperatures for the rest of the phases and structures analyzed throughout this subsection.

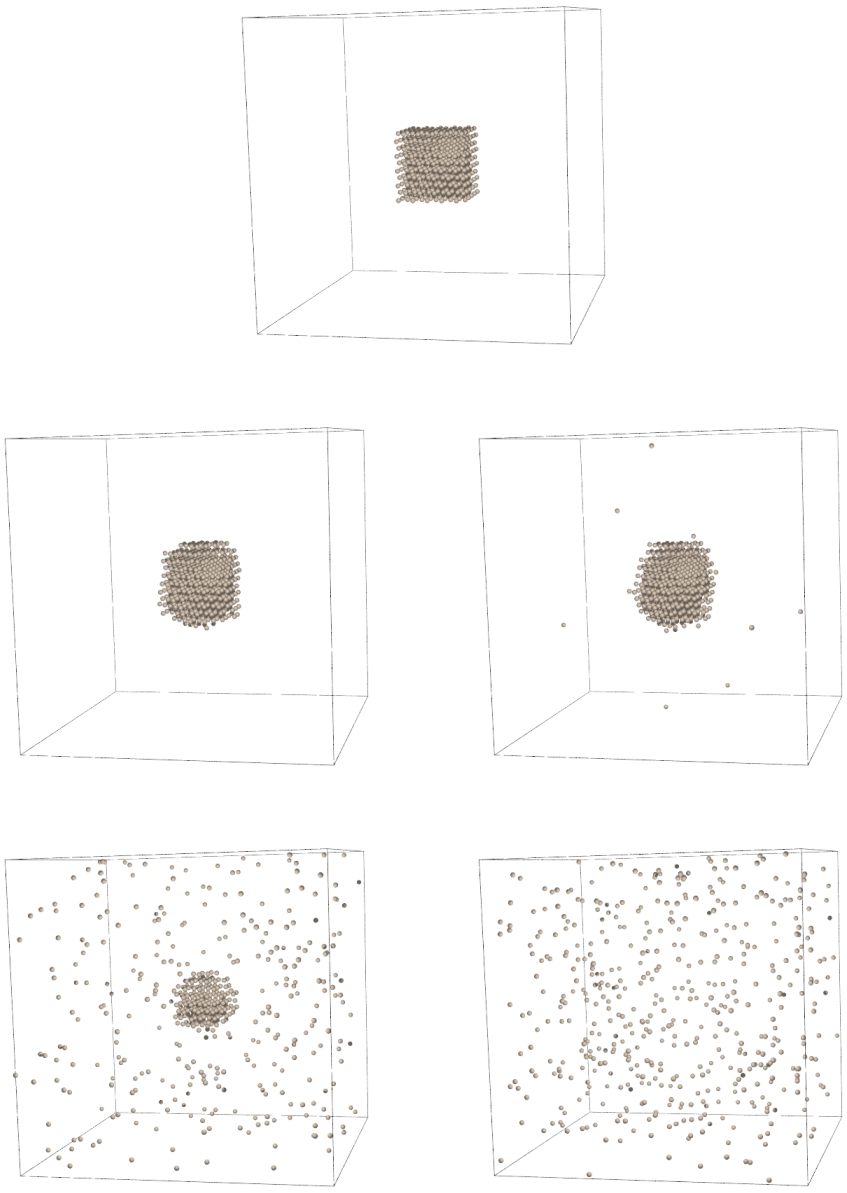

Figure 4.22: Dissolution of an Fe_3Si cube inside the larger iron encasement obtained with MC simulated heating. Only the silicon atoms are shown. The structure contains 500 silicon atoms. The following conditions are employed in the canonical ensemble from top to bottom, left to right: initial, 50 K, 150 K, 225 K, and 1000 K.

The dissolution process of an Fe_3Si octahedron is displayed in Figure 4.23. From the analysis of the SOP, it is known that the structure does not deform at 50 K, as is seen here. At 175 K the octahedron has lost its corners, and some silicon atoms have drifted into the iron surroundings. When the corners are removed, the (100) layers of the bcc structure are exposed. Even though these layers are the ones with the smallest atomic density the structure seems to favor this semi-spherical shape. At 250 K, the temperature is close to T_c. Here the sphere has reduced in size, as silicon atoms have started to randomly distribute in the iron encasement. Only a small part

of the initial Fe_3Si remains in the center at this temperature.

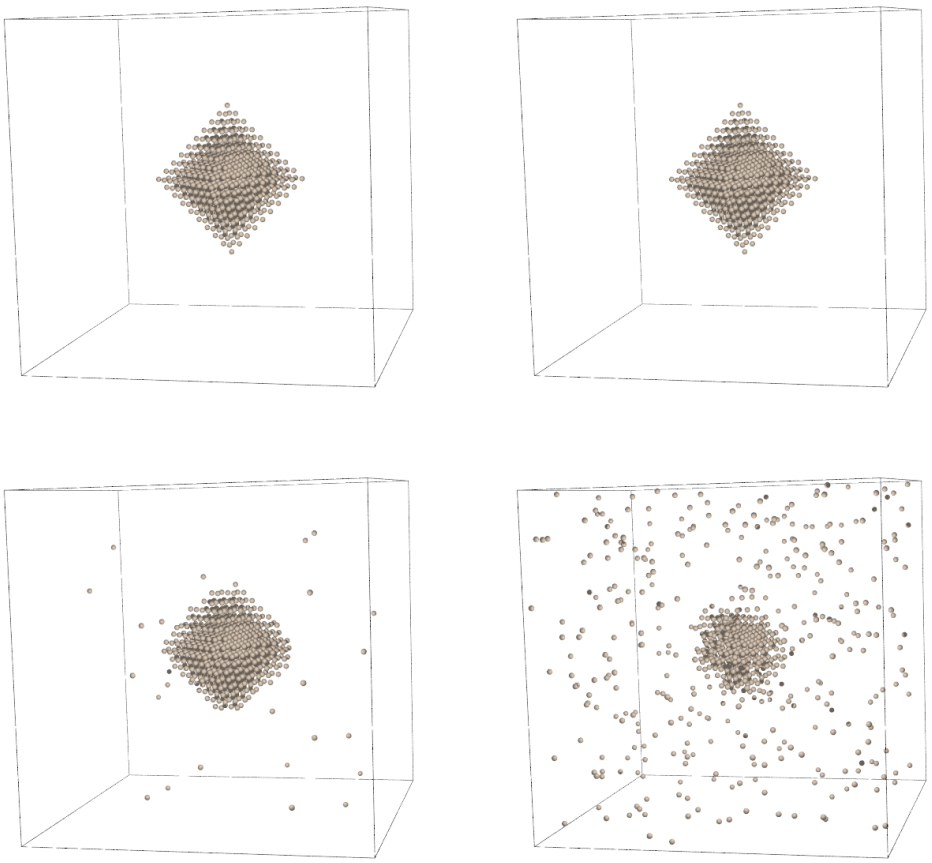

Figure 4.23: Dissolution of an Fe_3Si octahedron inside an iron encasement obtained with MC simulated heating. Only the silicon atoms are shown. The structure contains 670 silicon atoms. The following conditions are employed in the canonical ensemble from top to bottom, left to right: initial, 50 K, 175 K, and 250 K.

Next is an analysis of the FeSi phase dissolution. Figure 4.24 shows the effect on the interior silicon atoms in a cubic arrangement of FeSi for different temperatures. At 50 K some of the atoms on the edges of the cube have moved to the top and bottom of the structure, creating an oval shape. This process continues as the temperature reaches 600 K, and the oval shape is even more pronounced. Why the structure is elongated in this specific way is unknown, as the silicon atoms could have dissolved to create a more spherical shape. To further analyze this effect, several simulations of the same structure could be done, as only one simulation for this specific structure is done here. Therefore, no averages can be obtained to conclude on this. Some of the silicon atoms have also started to move into the surrounding iron cube at this temperature. At 750 K, the temperature is close to T_c, and the oval structure has become more spherical. The atoms located on the top and bottom of the structure are the first to dissolve into the iron surroundings.

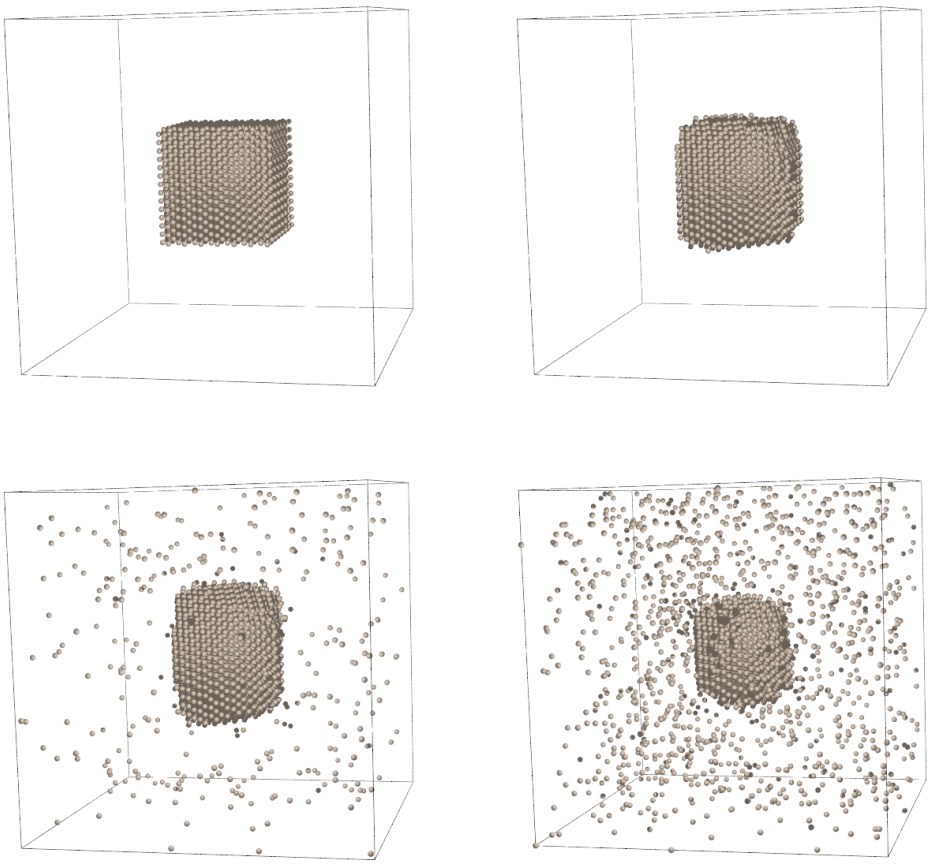

Figure 4.24: Dissolution of an FeSi cube inside an iron encasement obtained with MC simulated heating. Only the silicon atoms are shown. The structure contains 2788 silicon atoms. The following conditions are employed in the canonical ensemble from top to bottom, left to right: initial, 50 K, 600 K, and 750 K.

In Figure 4.25 the dissolution of an FeSi octahedron is shown. Comparing the initial structure and the structure at 50 K, the octahedron turns into a spherical shape for low temperatures, and no silicon atoms are dissolved towards the exterior. This structure requires much higher energy fluctuations before silicon atoms move into the iron surroundings, compared to the Fe_3Si octahedron, as this starts to happen at 450 K. From the analysis of the critical temperature it is known that this phase has a significantly higher T_c compared to that of the Fe_3Si phase. At 625 K the temperature is close to T_c, and the sphere has reduced in size, as silicon atoms on the outer perimeter of the structure have dissolved into the iron encasement.

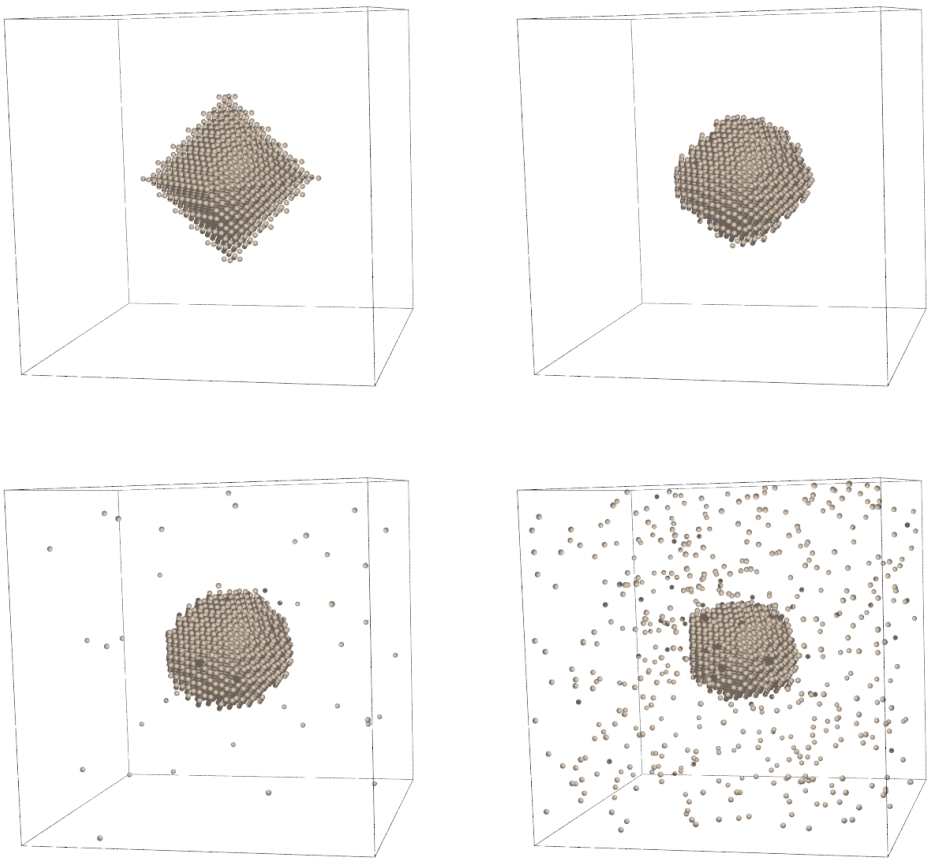

Figure 4.25: Dissolution of an FeSi octahedron inside an iron encasement obtained with MC simulated heating. Only the silicon atoms are shown. The structure contains 1904 silicon atoms. The following conditions are employed in the canonical ensemble from top to bottom, left to right: initial, 50 K, 450 K, and 625 K.

There are a few similarities between the four structures investigated here. At some temperature all structures deform to some kind of spherical shape. It is difficult to conclude why this happens, but it could be that the structures favor minimizing the ratio of surface area over volume. The silicon atoms on the corners of the initial structures are those that dissolve into the iron encasement first, or re-orients to positions which makes the internal structure have more of a spherical shape. These silicon atoms have the most iron atoms as nearest neighbors and second nearest neighbors in the initial structures, and seem to be the most mobile.

4.5.5 Phase boundary tracing

In this subsection, phase boundary tracing is done to obtain the iron-silicon phase diagram for silicon concentrations at 25 % and lower. All quantities needed to calculate the thermodynamic potential (2.83) for the phases are obtained by doing MC simulations in the semi-grand canonical ensemble with varying chemical potentials across multiple simulations. The number of MC steps done at each temperature is 1000 times the number of atoms in the structure, and the structures

are set to contain 8192 atoms in total. The chemical potentials used are close to the calculated $T \to 0$ limit of the chemical potential (2.87) for the Fe_3Si phase. For both the pure iron and Fe_3Si phase, an initial structure is created for the given phase, and the temperature is gradually increased from 100 K to 1200 K. The concentrations are allowed to vary as by the definition of the semi-grand canonical ensemble, as shown in Figure 4.26. To reduce computation time the simulations are stopped for the initial Fe_3Si phase if X(Si) < 0.15. Calculations for the Fe_3Si phase with $\mu \geq -1.25$ eV/atom does not extend up to 1200 K, as the simulations are stopped when concentrations move past this threshold. Figure 4.26 also reveals that for low temperatures the initial concentrations of the pure iron and the Fe_3Si phase, X(Si) $= 0$ and X(Si) $= 0.25$ respectively, are energetically favorable for the chemical potentials used in these calculations.

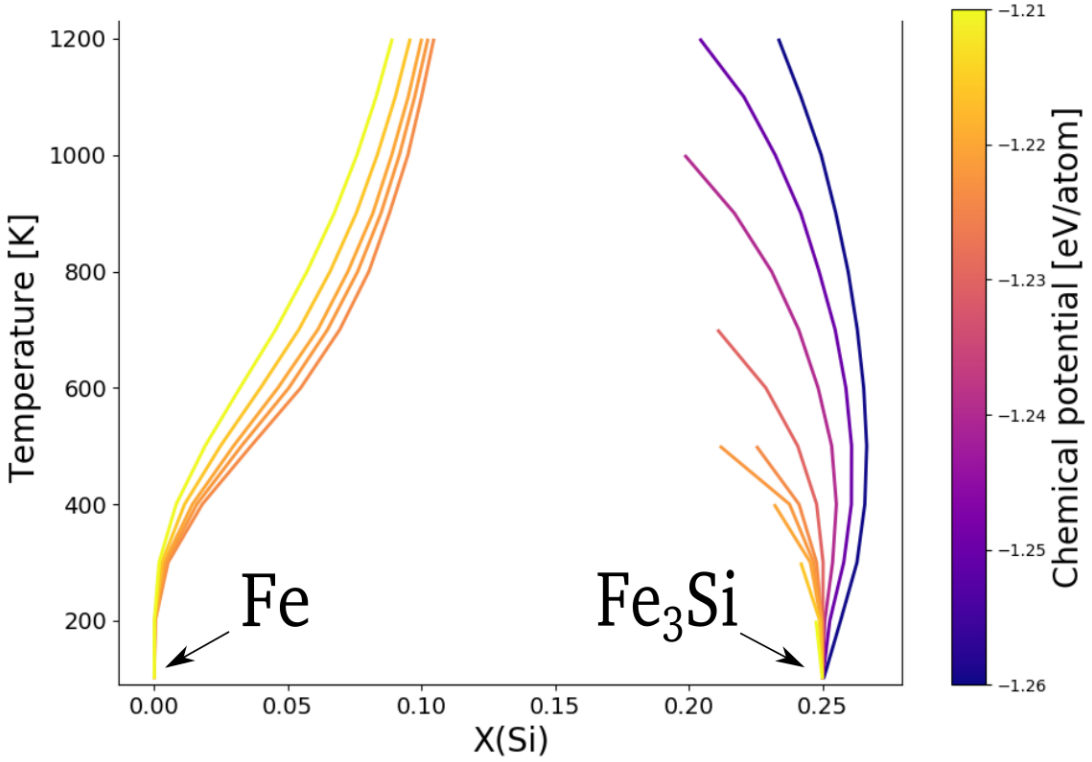

Figure 4.26: Temperature and concentration when heating an initial pure bcc iron structure and an initial Fe_3Si structure in the semi-grand canonical ensemble. The chemical potential is varied across calculations.

The phase boundary is obtained by finding concentrations and temperatures where the two phases co-exist. This is done by using the data from the MC simulations shown in Figure 4.26 and the corresponding energy for a given phase, temperature, T, and chemical potential, μ. The thermodynamic potentials (2.83) for the two phases are then calculated, to obtain T' and μ' such that $\beta\phi^{\mathrm{Fe}}(T', \mu') = \beta\phi^{\mathrm{Fe_3Si}}(T', \mu')$. This is the thermodynamic criteria for the two phases to co-exist. The temperature and chemical potential are then used to obtain X(Si) corresponding to these two parameters for both phases.

In Figure 4.27, the temperature as a function of silicon concentration is shown for the two phase

boundaries. To the left of the blue line either a pure iron phase or an iron phase with silicon atoms scattered randomly around is expected to be seen, depending on the temperature and concentration. Between the two boundaries, a combination of iron domains and Fe_3Si domains exists. The structure displayed in the figure for X(Si) = 0.1 supports this argument. This structure is obtained from simulated annealing in the canonical ensemble with X(Si) = 0.1, and it can be seen that this structure contains iron domains as well as domains of Fe_3Si. It is not possible to know to which degree the Fe_3Si domains cluster together based on these results. To the right of the red line for X(Si) $\leq$ 0.25 the Fe_3Si phase is present, with iron atoms scattered randomly around, depending on the concentration and temperature. For X(Si) $>$ 0.25 it is not possible to know which phase configuration is most favorable from these calculations.

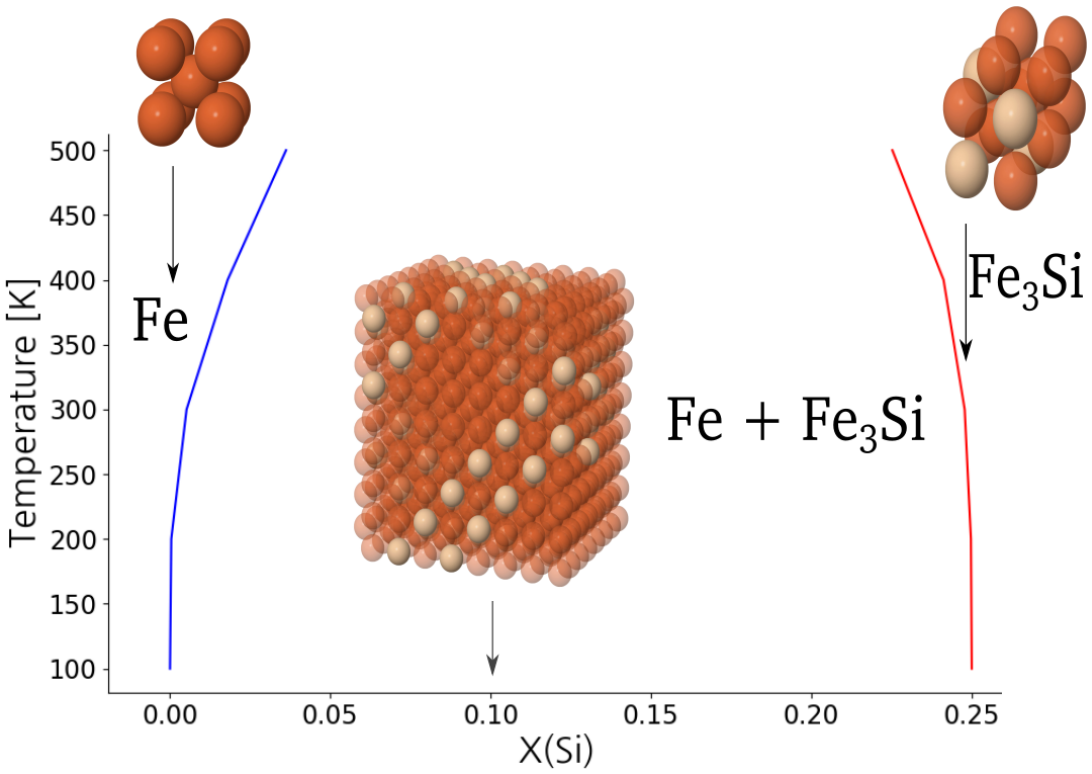

Figure 4.27: Temperature and concentration for the two phase boundaries from phase boundary tracing. Illustrations of structures at three concentrations are included.

4.6 Surface energy

This section presents the calculated surface energy associated with the intersect between the Fe_3Si and pure iron phases. The smallest cell representing the Fe_3Si structure contains 16 atoms, such that a one-layered structure consists of 32 atoms in total, where 16 are the Fe_3Si phase and 16 are the pure iron phase, as illustrated in Figure 4.28a. A two-layer structure is shown in Figure 4.28b. This structure is constructed in the same way, but the thickness of the Fe_3Si and the pure iron phases is doubled, creating a cell with twice the volume as for the one layer cell.

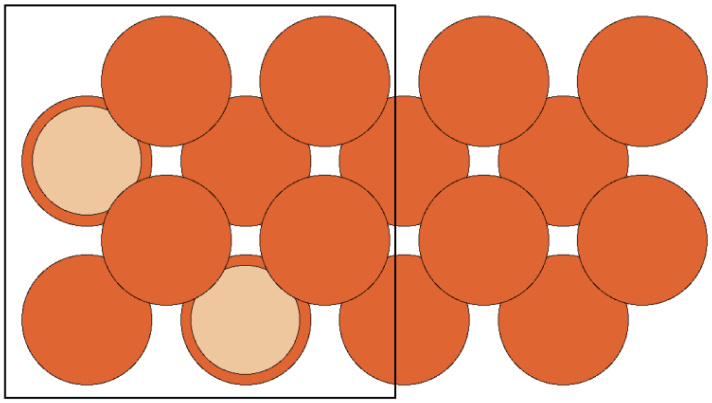

(a) One layer structure.

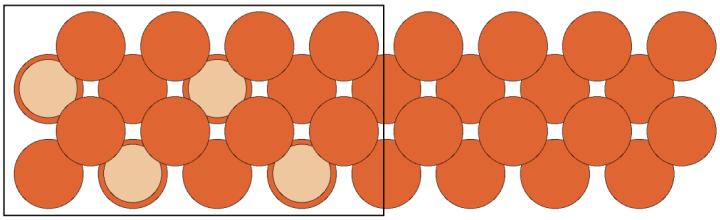

(b) Two layer structure.

Figure 4.28: Illustrations of the structures used for calculating the surface energy between the Fe_3Si phase and the iron phase. The structures are shown in the xy-plane. The Fe_3Si part of the structures are located within the black boundaries.

DFT calculations are done for the two structures as shown in Figure 4.28. The GPAW input parameters used in the calculations are as follows, $E_{\text{cut}} = 700$ eV, nbands $= -100$, $k_{\text{B}}T = 0.1$ eV and $k_{\text{dens}} = 5.4$ Å^{-1}. Periodic boundary conditions are applied in all directions, the PBE functional is used and the BFGS algorithm is employed to optimize the cell. Having obtained the slab energies for the one and two layer structures, the surface energy is calculated using Equation (2.28) with $n = 2$, as the larger structure is two layers thick. The surface energy per area between the Fe_3Si and pure iron phases is found to be $\gamma = 99.96$ mJ/m^2. $\gamma > 0$ indicates that energy is required for the two phases to mix together, essentially dissolving the silicon atoms from the Fe_3Si phase in the pure iron phase. This supports the argument that Fe_3Si domains could cluster together in a mixture of Fe_3Si and pure iron phases.

There are several methods for calculating the surface energy, and which method is appropriate to use depends on the system studied. The method used here requires only slab energies, and methods based on solely slab related quantities when calculating the surface energy are shown to converge for increasing layer thickness [58]. This is as opposed to methods for calculating the surface energy that relies on the the bulk energies for the pure separated phases, as with these methods the surface energy could diverge when the layer thickness is increased.

5 Conclusion

In short, various material properties of bcc iron and silicon alloys have been obtained by using computational methods based on DFT calculations from first principles. Concepts from within the fields of solid state physics and statistical physics have been employed to calculate desired attributes of the metals. The GGA xc functional used was the PBE functional. Suitable GPAW input parameters for doing energy calculations for different sized iron systems were obtained by doing total energy convergence tests. DFT calculations were shown to accurately predict the expected ferromagnetic ordering of iron, as well as the magnetic moment associated with each atom. For all except one structure, the iron-silicon alloys were found to have smaller or equal magnetic moment per atom compared to that of the pure iron system. The results obtained for the electronic band structure for bcc iron and diamond cubic silicon agreed well with previous works.

A total of 83 iron-silicon structures with silicon concentrations ranging from 0 % to 52.5 % were relaxed, and the DFT energies were used to develop a CE model. The model gave a CV score of 23.8 meV/atom. From the ECIs it was discovered that having iron and silicon atoms in nearest neighbor distance was favored for reducing the configurational energy. Two structures on the convex hull were identified at silicon concentrations of 25 % and 50 %. The CE model accurately predicted the energy of these structures.

MC simulated annealing in the canonical ensemble predicted the same structure as identified on the convex hull for a silicon concentration of 25 %. For a silicon concentration of 50 %, the MC method found a different structure than the one on the convex hull at this concentration. The structure predicted by MC had alternating silicon and iron planes in the (110) directions, while the one on the convex hull had planes in the (100) directions. These two systems were found to have similar formation energies. The dissolution of the two ground state phases predicted by MC simulated annealing in an iron encasement was further studied. It was discovered that the FeSi phase required higher temperatures to dissolute in iron surroundings compared to the temperatures needed to dissolute the Fe_3Si phase. The two phases placed in the interior of the pure iron phase were constructed as both cubes and octahedra of similar size. For the FeSi phase, it was discovered that the octahedra were more stable than the cubes when subjected to the same temperatures. This was also found to be the case for smaller structures of the Fe_3Si phase.

Phase boundary tracing was done for silicon concentrations from 0 % to 25 %. From these calculations, the phase diagram in this concentration interval was obtained, identifying a temperature and concentration region in which the pure iron phase co-existed with the Fe_3Si phase.

Lastly, the surface energy associated with an interface between a pure iron phase and the Fe_3Si phase was found to be $\gamma = 99.96$ mJ/m^2. This result supported the claim that the Fe_3Si phase can exist as clusters in pure iron surroundings.

6 Future work

It would be interesting to expand the iron-silicon phase diagram for higher silicon concentrations. Doing this would at some point require calculating a new set of DFT data and obtain new ECIs for iron-silicon structures on other lattices. This is due to silicon having a diamond cubic lattice structure. Other lattice types could also be examined, as there may exist stable or meta-stable iron-silicon phases on lattice types which are not bcc or diamond cubic.

Ferrosilicon alloys are often used as inoculants when making cast iron [59], and carbon is added in the manufacturing process of this material. Introducing carbon in the alloy changes the brittleness and rigidity of the compound. Further analysis of iron, silicon, and carbon could reveal interesting aspects about cluster formation observed in experiments [60] and the dissolution of Fe_3Si and FeSi clusters in iron-carbon encasements. The size and shape of these clusters affect the macroscopic properties of the final product.

One drawback of the CE method used in this thesis is that no information can be obtained about the magnetic properties of the iron-silicon alloy. Neglecting the magnetic moments of the individual atoms could affect the results obtained from MC simulations, as iron-silicon alloys are known to have magnetic phase transitions [56, p. 711]. With the use of neural networks, the magnetic moments of alloys obtained by DFT could be used as additional input data for predicting the magnetic properties of an alloy [61]. It should be noted that the CE method used in this thesis could be further developed to make use of the magnetic moments calculated by DFT.

References

[1] T. M. Green, *The Greek & Latin Roots of English*. Rowman & Littlefield, 2014.

[2] *Elkem website*, `https://www.elkem.com/foundry/foundry-and-steel-products/special-silicon-ferroalloys/`, Accessed: 2019-06-10.

[3] C. E. Dremann,
Magnesium ferrosilicon alloy and use thereof in manufacture of modular cast iron,
US Patent 4,385,030, 1983.

[4] H. Fredriksson, "Inoculation of iron-base alloys,"
Materials Science and Engineering, vol. 65, no. 1, pp. 137–144, 1984, Solidification Microstructure: 30 Years after Constitutional Supercooling.

[5] R. O. Jones, "Density functional theory: Its origins, rise to prominence, and future,"
Rev. Mod. Phys., vol. 87, no. 3, pp. 897–923, 2015.

[6] J. Sanchez, "Cluster expansions and the configurational energy of alloys,"
Physical review. B, Condensed matter, vol. 48, pp. 14 013–14 015, 1993.

[7] D. Kleiven *et al.*, "Atomistic simulations of early stage clusters in almg alloys,"
Acta Materialia, vol. 166, pp. 484–492, 2019.

[8] C. Kittel, *Introduction to Solid State Physics*. 8th ed, John Wiley & Sons, Inc, 2005.

[9] W. Setyawan and S. Curtarolo, "High-throughput electronic band structure calculations: Challenges and tools," *Computational Materials Science*, vol. 49, no. 2, pp. 299–312, 2010.

[10] R. M. Martin, *Electronic Structure: Basic Theory and Practical Methods*.
Cambridge University Press, 2004.

[11] J. O. Andersen, *Introduction to statistical mechanics*. Trondheim: Akademika forlag, 2012.

[12] V. Gupta, "12 - characterization of chemical reactions,"
in *Principles and Applications of Quantum Chemistry*, V. Gupta, Ed.,
Boston: Academic Press, 2016, pp. 385–433.

[13] P. C. Hemmer, *Termisk fysikk*, 2nd. Tapir Akademisk Forlag, 1989.

[14] A. Mitsos and P. I. Barton, "A dual extremum principle in thermodynamics,"
AIChE Journal, vol. 53, no. 8, pp. 2131–2147, 2007.

[15] D. Hildebrandt, "Predicting phase and chemical equilibrium using the convex hull of the gibbs free energy," *The Chemical Engineering Journal and The Biochemical Engineering Journal*, vol. 54, pp. 187–197, 1994.

[16] C. D. Marioara *et al.*, "Improving thermal stability in cu-containing al-mg-si alloys by precipitate optimization,"
Metallurgical and Materials Transactions A, vol. 45, no. 7, pp. 2938–2949, 2014.

[17] J. C. Boettger, "Nonconvergence of surface energies obtained from thin-film calculations," *Phys. Rev. B*, vol. 49, pp. 16 798–16 800, 23 1994.

[18] M. Born and R. Oppenheimer, "Zur Quantentheorie der Molekeln," *Annalen der Physik*, vol. 389, pp. 457–484, 1927.

[19] P. Hohenberg and W. Kohn, "Inhomogeneous electron gas," *Phys. Rev.*, vol. 136, no. 3B, B864–B871, 1964.

[20] M. Levy, "Universal variational functionals of electron densities, first-order density matrices, and natural spin-orbitals and solution of the v-representability problem," *Proceedings of the National Academy of Sciences of the United States of America*, vol. 76, pp. 6062–5, 1980.

[21] E. H. Lieb, "Density functionals for coulomb systems," *International Journal of Quantum Chemistry*, vol. 24, pp. 243–277, 1983.

[22] W. Kohn and L. J. Sham, "Self-consistent equations including exchange and correlation effects," *Phys. Rev.*, vol. 140, no. 4A, A1133–A1138, 1965.

[23] S. K. Ma and K. A. Brueckner, "Correlation energy of an electron gas with a slowly varying high density," *Phys. Rev.*, vol. 165, no. 1, pp. 18–31, 1968.

[24] J. P. Perdew, K. Burke, and M. Ernzerhof, "Generalized gradient approximation made simple," *Phys. Rev. Lett.*, vol. 77, no. 18, pp. 3865–3868, 1996.

[25] A. van de Walle and G. Ceder, "Automating first-principles phase diagram calculations," *Journal of Phase Equilibria*, vol. 23, no. 4, p. 348, 2002.

[26] S. Derin Babacan, R. Molina, and A. Katsaggelos, "Bayesian compressive sensing using laplace priors," *IEEE Transactions on Image Processing*, vol. 19, pp. 53–63, 2010.

[27] D. L. Donoho, "Compressed sensing," *IEEE Transactions on Information Theory*, vol. 52, no. 4, pp. 1289–1306, 2006.

[28] D. Chandler, "Introduction to modern statistical mechanics," *New York: Oxford University Press*, 1987.

[29] W. K. Hastings, "Monte carlo sampling methods using markov chains and their applications," *Biometrika*, vol. 57, no. 1, pp. 97–109, 1970.

[30] A. van de Walle and M. Asta, "Self-driven lattice-model monte carlo simulations of alloy thermodynamic properties and phase diagrams," *Modelling and Simulation in Materials Science and Engineering*, vol. 10, no. 5, pp. 521–538, 2002.

[31] J. Enkovaara *et al.*, "Gpaw - massively parallel electronic structure calculations with python-based software," *Procedia Computer Science*, vol. 4, pp. 17–25, 2011.

[32] J. J. Mortensen, L. B. Hansen, and K. W. Jacobsen, "Real-space grid implementation of the projector augmented wave method," *Phys. Rev. B*, vol. 71, no. 3, p. 035 109, 2005.

[33] J. Enkovaara *et al.*, "Electronic structure calculations with gpaw: A real-space implementation of the projector augmented-wave method," *Journal of physics. Condensed matter : an Institute of Physics journal*, vol. 22, p. 253 202, 2010.

[34] G. Kresse and J. Furthmüller, "Efficiency of ab-initio total energy calculations for metals and semiconductors using a plane-wave basis set,"
Computational Materials Science, vol. 6, no. 1, pp. 15–50, 1996.

[35] A. H. Larsen *et al.*, "The atomic simulation environment-a python library for working with atoms.," *Journal of physics. Condensed matter : an Institute of Physics journal*, vol. 29 27, p. 273 002, 2017.

[36] C. L. Lawson *et al.*, "Basic linear algebra subprograms for fortran usage,"
ACM Trans. Math. Softw., vol. 5, no. 3, pp. 308–323, 1979.

[37] L. S. Blackford *et al.*, *ScaLAPACK User's Guide*, J. J. Dongarra, Ed.
Philadelphia, PA, USA: Society for Industrial and Applied Mathematics, 1997.

[38] L. Prechelt, "An empirical comparison of seven programming languages,"
Computer, vol. 33, pp. 23–29, 2000.

[39] P. Pacheco, *An Introduction to Parallel Programming*, 1st.
San Francisco, CA, USA: Morgan Kaufmann Publishers Inc., 2011.

[40] K. Ryczko, D. Strubbe, and I. Tamblyn, "Deep learning and density functional theory,"
arXiv preprint arXiv:1811.08928, 2018.

[41] H. J. Monkhorst and J. D. Pack, "Special points for brillouin-zone integrations,"
Phys. Rev. B, vol. 13, no. 12, pp. 5188–5192, 1976.

[42] M. A. Marques, M. J. Oliveira, and T. Burnus, "Libxc: A library of exchange and correlation functionals for density functional theory,"
Computer Physics Communications, vol. 183, no. 10, pp. 2272–2281, 2012.

[43] J. P. Perdew and Y. Wang, "Accurate and simple analytic representation of the electron-gas correlation energy," *Phys. Rev. B*, vol. 45, no. 23, pp. 13 244–13 249, 1992.

[44] J. P. Perdew and A. Zunger, "Self-interaction correction to density-functional approximations for many-electron systems,"
Phys. Rev. B, vol. 23, no. 10, pp. 5048–5079, 1981.

[45] D. C. Liu and J. Nocedal, "On the limited memory bfgs method for large scale optimization," *Mathematical Programming*, vol. 45, no. 1, pp. 503–528, 1989.

[46] D. Packwood *et al.*, "A universal preconditioner for simulating condensed phase materials," *The Journal of Chemical Physics*, vol. 144, p. 164 109, 2016.

[47] J. H. Chang *et al.*, "Clease: A versatile and user-friendly implementation of cluster expansion method,"
Journal of Physics: Condensed Matter, vol. 31, no. 32, p. 325 901, 2019.

[48] D. Hildebrandt and D. Glasser, "Predicting phase and chemical equilibrium using the convex hull of the gibbs free energy," *The Chemical Engineering Journal and the Biochemical Engineering Journal*, vol. 54, no. 3, pp. 187–197, 1994.

[49] D. Kleiven, *Monte carlo package targeted at systems studied with the cluster expansion*, `https://github.com/davidkleiven/CEMC`, Accessed: 2019-05-30, 2019.

[50] J. Kübler, "Magnetic moments of ferromagnetic and antiferromagnetic bcc and fcc iron," *Physics Letters A*, vol. 81, no. 1, pp. 81–83, 1981.

[51] V. Moruzzi, J. Janak, and A. Williams, *Calculated Electronic Properties of Metals*. Elsevier Science & Technology Books, 1978.

[52] Y. Yao *et al.*, "First principles calculation of anomalous hall conductivity in ferromagnetic bcc fe," *Physical review letters*, vol. 92, p. 037 204, 2004.

[53] R. Benchamekh *et al.*, "Microscopic electronic wave function and interactions between quasiparticles in empirical tight-binding theory," *Physical Review B*, vol. 91, p. 045 118, 2015.

[54] V. Blum and A. Zunger, "Mixed-basis cluster expansion for thermodynamics of bcc alloys," *Phys. Rev. B*, vol. 70, p. 155 108, 15 2004.

[55] U. Starke *et al.*, "Structural and compositional reversible phase transitions on low-index fe3si surfaces," *EPL (Europhysics Letters)*, vol. 56, p. 822, 2007.

[56] M. Hansen, K. Anderko, and R. Elliott, *Constitution of Binary Alloys*, ser. McGraw-Hill series in materials science and engineering. McGraw-Hill, 1958.

[57] T. Sauer, *Numerical Analysis*, 2nd. Pearson Addison Wesley, 2006.

[58] V. Fiorentini and M. Methfessel, "Extracting convergent surface energies from slab calculations," *Journal of Physics: Condensed Matter*, vol. 8, no. 36, pp. 6525–6529, 1996.

[59] *Elkem inoculants*, `https://www.elkem.com/foundry/foundry-and-steel-products/inoculants2/`, Accessed: 2019-06-14.

[60] D. Stefanescu *et al.*, "On the crystallization of graphite from liquid iron-carbon-silicon melts," *Acta Materialia*, vol. 107, pp. 102–126, 2016.

[61] J. Nelson, R. Tiwari, and S. Sanvito, "Machine learning density functional theory for the hubbard model," *Physical Review B*, vol. 99, 2019.

Appendix A

Table A1: Number of structures with the same number of atoms included in the CE model.

Number of atoms in the structures	Number of structures used in the CE
2	1
4	4
6	10
8	17
9	5
16	6
27	40

NTNU

Kunnskap for en bedre verden